Imaging Mofette Structures in the Ohře Rift System, Czech Republic, Using Radio-Magnetotelluric Data

Rulff, Paula; Weckmann, Ute; Kalscheuer, Thomas; Willkommen, Gregor; Buntin, Laura Maria; Platz, Anna

DOI
10.1007/s00024-025-03665-7

Publication date
2025

Document Version
Final published version

Published in
Pure and Applied Geophysics

Pure Appl. Geophys.

https://doi.org/10.1007/s00024-025-03665-7

Pure and Applied Geophysics

Imaging Mofette Structures in the Ohře Rift System, Czech Republic, Using Radio-Magnetotelluric Data

Paula Rulff,[1,2,3,4] Ute Weckmann,[2,3] Thomas Kalscheuer,[1] Gregor Willkommen,[2,3,5] Laura Maria Buntin,[1] and Anna Platz[2]

Abstract—The pathways of fluids and mantle-originated carbon dioxide in the seismically active Ohře (Eger) Rift system appearing as mofettes at the surface are currently subject to investigation, especially by the International Continental Scientific Drilling Program "Drilling the Eger Rift". If the aquifers show significant contrast in electrical resistivity to the host rocks, they can be investigated with geo-electromagnetic methods. However, imaging complex fluid and CO_2 pathways in detail in near-surface structures is challenging, because, in contrast to the background stratigraphy, they are often oriented in near-vertical directions. Therefore, we aim to investigate how the shallow aquifer structures can be examined best with an inductive electromagnetic method. For this purpose, we collected radio-magnetotelluric data in the Hartoušov mofette field and evaluated them by two- and three-dimensional inversions. Data from a nearby magnetotelluric station, drill hole data, gas flux measurements and electrical resistivity tomography models were used to assess the reliability and robustness of our inversion results. We concluded that the near-surface fluid reservoirs are adequately depictable, while the migration paths of gaseous CO_2 cannot be traced properly due to a lack of resistivity contrast. Our model analyses suggest that imaging the given geological setting with fluids and gases ascending in anastomosing pathways benefits from a fine-scale three-dimensional inversion approach because the fluids mostly appear as local conductive reservoir-like anomalies, which can be falsely projected onto the profiles during inversion in two dimensions. The resistivity models contribute with detailed images of the near-surface aquifers to the geodynamic model of the Ohře Rift.

Keywords: Radio-magnetotellurics, inversion, aquifer.

1. Introduction

The intraplate stress field caused by the Alpine orogenesis formed the ENE-striking Ohře Graben located in the western Czech Republic (Fig. 1a, b) in the Tertiary (e.g. Prodehl et al., 1995). Earthquake swarms up to magnitude $M < 4.5$ triggered by uprising mantle fluids occur periodically and indicate ongoing magmatic activity in the lithospheric mantle (Fischer et al., 2014). The mofette structures of the Hartoušov mofette field (HMF) in the western Ohře Rift system (Fig. 1b, c) are evidence for active magmatism at the surface.

The mofette structures are degassing sites of natural CO_2 which is created by magmatic processes in the lithospheric mantle (e.g. Bräuer et al., 2008). In recent years, the mofettes have become a topic of interest, because they can be used as natural test sites to identify suitable methods for monitoring the propagation of fluids and CO_2 through the subsurface (Schütze et al., 2012).

Several geological, geochemical and geophysical methods have been applied to study the mofettes in the Ohře Rift and the surrounding geological structures in order to understand the geodynamic phenomena observed in this area (e.g. Bräuer et al., 2009; Bussert et al., 2017; Flores Estrella et al., 2016; Nickschick et al., 2015). To determine the relations between the seismic activity and the geodynamic processes, seismological studies were performed (Bankwitz et al., 2003; Růzek & Horálek, 2013). Seismic noise tomography was used to locate fluids and pathways of the mantle-derived gas (Flores Estrella et al., 2016). Soil-gas investigations such as concentration and flux as well as isotope

[1] Department of Earth Sciences, Uppsala University, Uppsala, Sweden. E-mail: P.Rulff@tudelft.nl
[2] Helmholtz Centre Potsdam, German Research Centre for Geoscience (GFZ), Potsdam, Germany.
[3] University of Potsdam, Institute of Geosciences, Potsdam, Germany.
[4] Faculty of Engineering and Geosciences, TU Delft, Delft, The Netherlands.
[5] Bundesanstalt für Geowissenschaften und Rohstoffe (BGR), Berlin, Germany.

Published online: 03 February 2025

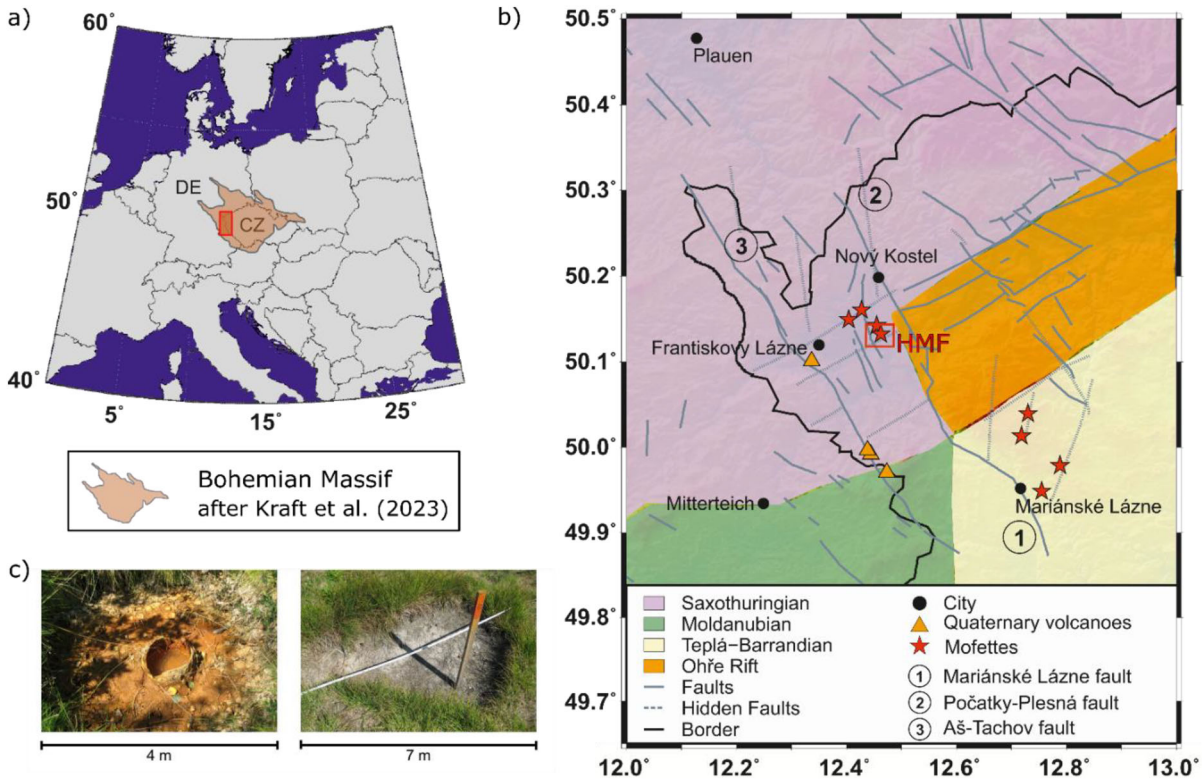

Figure 1

a The location of the Bohemian Massif (brown shaded area, after Kraft et al. 2023) and the area of interest (red rectangle) within central Europe. **b** Geological overview map showing the geological units and features of the region. The red rectangle marks the study area, i.e. the Hartoušov mofette field (HMF). **c** Photo of a wet mofette (left) and dry mofette (right) in the HMF

measurements aimed to quantify the CO_2 emissions and to determine its origin (Kämpf et al., 2007, 2019; Nickschick et al., 2015). Understanding the structure and sedimentological composition of the mofettes and the time variability of the gas flux was the motivation to perform electric resistivity tomography (ERT), self-potential and soil gas measurements (Flechsig et al., 2008; Nickschick et al., 2015, 2017, 2019; Sauer et al., 2014). The most recent studies within the International Continental Scientific Drilling Program "Drilling the Eger Rift" (Daskalopoulou et al., 2021; Fischer et al., 2022; Woith et al., 2022) provide, amongst other findings, further insights into the chemical composition of the ascending gases and fluids.

Some published data and results are directly used for an integrated interpretation in our study: a magnetotelluric (MT) survey performed by Munoz et al. (2018), ERT measurements (Sauer et al., 2014), soil gas measurements (Nickschick et al., 2015) and data from drilling logs (Bussert et al., 2017; Sauer et al., 2014). These studies indicate that CO_2-rich gases and mineral fluids with dissolved and gaseous CO_2 migrating through the subsurface geochemically or geothermally alter the properties of the subsurface and can create significant resistivity contrasts to the surrounding soil or rock.

The motivation for this study is to investigate the potential of an inductive electromagnetic (EM) method to image near-surface structures related to ascending gas and fluids in detail. Whereas broadband MT (Aleid et al., 2022; Mair, 2020; Muñoz et al., 2018; Platz et al., 2022) was already successfully performed in an extended area around the mofette fields, a high-frequency inductive method has not been tested in the mofette fields yet. Regional 3D MT models reveal reservoir-like conductive features at depth (approx. 10–28 km) laterally offset (Platz

et al., 2022) and potentially connected to local highly conductive (< 20 Ωm) near-surface anomalies at the mofette fields within a sedimentary basin characterised by a moderate conductive anomaly (20–200 Ωm) down to 125–250 m depth. Conductive anomalies (< 80 Ωm) are likely to image the locations and potential pathways of fluids and gas (closer to the surface) and a single-phase fluid system with dissociated ions and magma (at larger depths). The crystalline basement is characterised by high resistivities (up to 57,000 Ωm). Complementing the MT studies with high-frequency EM measurements has the potential to resolve near-surface conductivity structures, which are difficult to image with the typical wide station spacing and the low frequency range of MT measurements. Therefore, we performed radio-magnetotelluric (RMT) measurements above mofette structures in the Hartoušov mofette field located in the western Czech Republic.

The RMT technique is an inductive EM method that uses EM field variations in a frequency range of 1 kHz to 3 MHz (Bastani, 2001) as signal. Radio or VLF transmitters as well as electric or magnetic dipole sources can emit these EM variations. Similar to other EM methods, RMT can be applied to image the electrical conductivity distribution of the shallow subsurface. The EM signal is measured at the Earth's surface with three magnetic field sensors (induction coils) and two pairs of electric field sensors that are inductively and galvanically coupled through sensor wires and/or electrodes at the ends of the wires, respectively. RMT transfer functions subsume impedance tensors (**Z**) and vertical magnetic transfer functions (VMTF or induction vectors) and can be estimated from the measured time series of the EM field components at selected frequencies. The complex impedance tensor is often represented as apparent resistivities and phases of its individual components. The RMT technique as well as related early publications are described in detail in Tezkan (2009). More recently, studies on successful applications of the RMT method to investigate the near-surface conductivity for environmental aspects, such as groundwater contamination and aquifer mapping, were reported by e.g. Yogeshwar et al. (2012), Saraev et al. (2020) and Vizheh et al. (2020). RMT models imaging the near-surface geology and fault-zones were published by Özyıldırım et al. (2017) and Bastani et al. (2021). In addition, the method has been used in the field of natural hazards, e.g., by Wang et al. (2016) to characterise a quick clay site.

RMT is predominantly sensitive to electrically conductive subsurface anomalies which are, in the geological setting of this work, mineralised fluids containing CO_2-rich gases. Moreover, we see potential in evaluating our RMT data in combination with a method that can image the same physical parameter (i) down to greater depth (MT) or (ii) that is primarily sensitive to resistive structures and contrasts (ERT). With this study, we want to obtain detailed near-surface models of the electric resistivity distribution below wet and dry mofette sites to image the preferred migration paths of CO_2 bearing fluids.

As local geology and published ERT resistivity models (e.g. Nickschick et al., 2015, 2019) suggest a predominantly layered structure of the shallow subsurface, it can be expected that a 2D inversion approach would be able to explain the collected RMT data sufficiently. However, Platz et al. (2022) highlight the importance of a 3D inversion approach for their MT models of the region to properly locate deep fluid reservoirs. Since we measured our RMT data exactly above mofette structures, the local fluid migration paths might introduce 3-D signatures into our data. Therefore, and to be able to assess the reliability of our resistivity models by cross-comparison, we evaluate our RMT data in 2D and 3D using two different inversion algorithms.

2. Geological Setting

2.1. The Ohře Rift System

The Ohře Rift System is located in the West Bohemian Massif (Fig. 1a, b). The Bohemian Massif is basically made up of Pre-Permian rocks and represents one of the largest stable outcrops of these rocks in Central and Western Europe. The Bohemian Massif developed between 500 and 250 Ma ago during the Variscan cycle, a period of large-scale crustal convergence, collision of continental plates and microplates, and subduction (e.g. Matte et al., 1990). The study area in the West Bohemian Massif

(Fig. 1b) is located within the transition zone of three tectonic units of the Variscan Belt, which are separated by sutures and fault zones: (i) the Saxothuringian Unit, (ii) the Teplá-Barrandian and (iii) the Moldanubian unit (Bräuer et al., 2014; Geissler et al., 2005; Matys Grygar et al., 2016). Since the Lower Triassic the Palaeozoic sutures between the Saxothuringian and Teplá-Barrandian/Moldanubian units have been reactivated repeatedly as a result the Alpine collision (Ziegler, 1992). Intraplate stress caused by the Alpine collision as well as alkaline magmatic activity during the Cenozoic led to the development of the NE-SW trending Ohře Rift. Nowadays, the Ohře Rift is 300 km long and 70 km wide. It is located at the northern border of the Bohemian Massif and separates the Saxothuringian Unit in the north from the Teplá-Barrandian Unit in the south. Furthermore, the Ohře Rift is part of the seismically active European Cenozoic Rift System (ECRIS; Prodehl et al., 1995) and represents its easternmost termination. The N-S trending Regensburg-Leipzig-Rostock Zone (RLRZ) is another prominent tectonic structure in the western part of the Bohemian Massif. The RLRZ is 700 km long and 40 km wide and consists of a network of many local faults (Bankwitz et al., 2003). The most important faults of the RLRZ in the study area are the NNW-striking approximately 100 km long Mariánské Lázně fault (MLF) zone, the Počatky-Plesná fault zone (PPZ) and the Aš-Tachov fault zone (Bankwitz et al., 2003). At the NW corner of the Bohemian Massif, a small intra-cratonic basin—the Cheb Basin—developed in the Upper Tertiary (Bankwitz et al., 2003). It represents the western termination of the Ohře Graben (Bankwitz et al., 2003) and is the youngest geological feature in northwest Bohemia.

The western part of the Bohemian Massif belongs to one of the geodynamically most active regions within central Europe; ongoing magmatic processes, that take place in the intra-continental lithospheric mantle, characterise the entire area. In absence of active volcanism at the surface, active tectonics is mainly manifested by Cenozoic volcanism (Ulrych et al., 2000), represented by several Quaternary volcanic structures in the Cheb Basin (Mrlina et al., 2009; Rohrmüller et al., 2017; Weinlich et al., 1999), and neotectonic crustal movements (Bankwitz et al., 2003; Schunk et al., 2005). Furthermore, the ongoing magmatic processes are expressed by a series of phenomena as the occurrence of repeated earthquake swarms of ML > 4 (e.g. Horálek & Fischer, 2008; Ulrych et al., 2011) and the massive degassing of CO_2 in the form of wet and dry mofettes (such as the Bublák or the Hartoušov mofette field; e.g. Nickschick et al., 2015) as well as CO_2-rich mineral springs.

2.2. *Mofette Structures*

The Hartoušov mofette field (HMF) is located in the westernmost part of the Ohře Rift System (Fig. 1b) within the sedimentary Cheb Basin. The mofettes occur as dry degassing sites and in combination with aqueous springs (Fig. 1c). The gas consists mainly of CO_2, but it contains also a small amount of helium carrying an isotopic signature from the upper mantle (Geissler et al., 2005; Nickschick et al., 2015; Weinlich et al., 1999). The location of the mofette structures near prominent fault zones (Fig. 1b) indicates preferential magmatic CO_2 migration pathways through the subsurface (Sauer et al., 2014). The gas ascends along en-echelon faults acting as fluid channels and CO_2 conduits inside the main local tectonic fault zone, the Počátky-Plesná Fault Zone, from the upper mantle to the surface (Kämpf et al., 2007, 2019). How the mofette fields are connected to the regional geologic features, such as volcanic structures and faults, is currently under scientific investigation.

A conceptual surface model of degassing structures as they occur in the HMF shows small mounds with depressions on top at locations of the strongest gas flow (Flechsig et al., 2008). Wet mofettes can be found at the surface as localised small-scale CO_2-rich mineral springs. Dry mofettes are indicated by extremely stressed vegetation, e.g. brown, dry grass (Flechsig et al., 2008; Kämpf et al., 2019; Sauer et al., 2014). Both types of mofette structures can exhibit a contrast in resistivity to their surrounding sand- and claystone stratigraphy in the Cheb basin. Whereas mineral fluids containing CO_2 show low electrical resistivities (Bussert et al., 2017), high electrical resistivities are expected in rocks the pore spaces of

which are filled with gaseous CO_2 (Nickschick et al., 2015; Yang et al., 2015).

3. Methodology

3.1. Data

We collected RMT data at 71 stations (Rulff, 2018) in summer 2017 in the northern HMF along three profiles directed − 40° N with a station distance of approximately 10 m (Fig. 2). The exact station locations were determined with a differential GPS system. The electric field was measured in two orthogonal horizontal directions in such a way, that the Ex-component was aligned perpendicular and the Ey-component parallel to the profile direction using a dipole length of 5 m. The magnetic field sensor, composed of three induction coils measuring the two horizontal components (Hx and Hy) and the vertical component (Hz) of the magnetic field, was placed accordingly. The profiles cover an area with anomalously high surface gas flux. The most prominent mofette structures are clearly visible at the surface.

Electric and magnetic field components from radio transmitters in a frequency range between 14 and 250 kHz were recorded using the EnviroMT instrument (Bastani, 2001; Bastani & Pedersen,

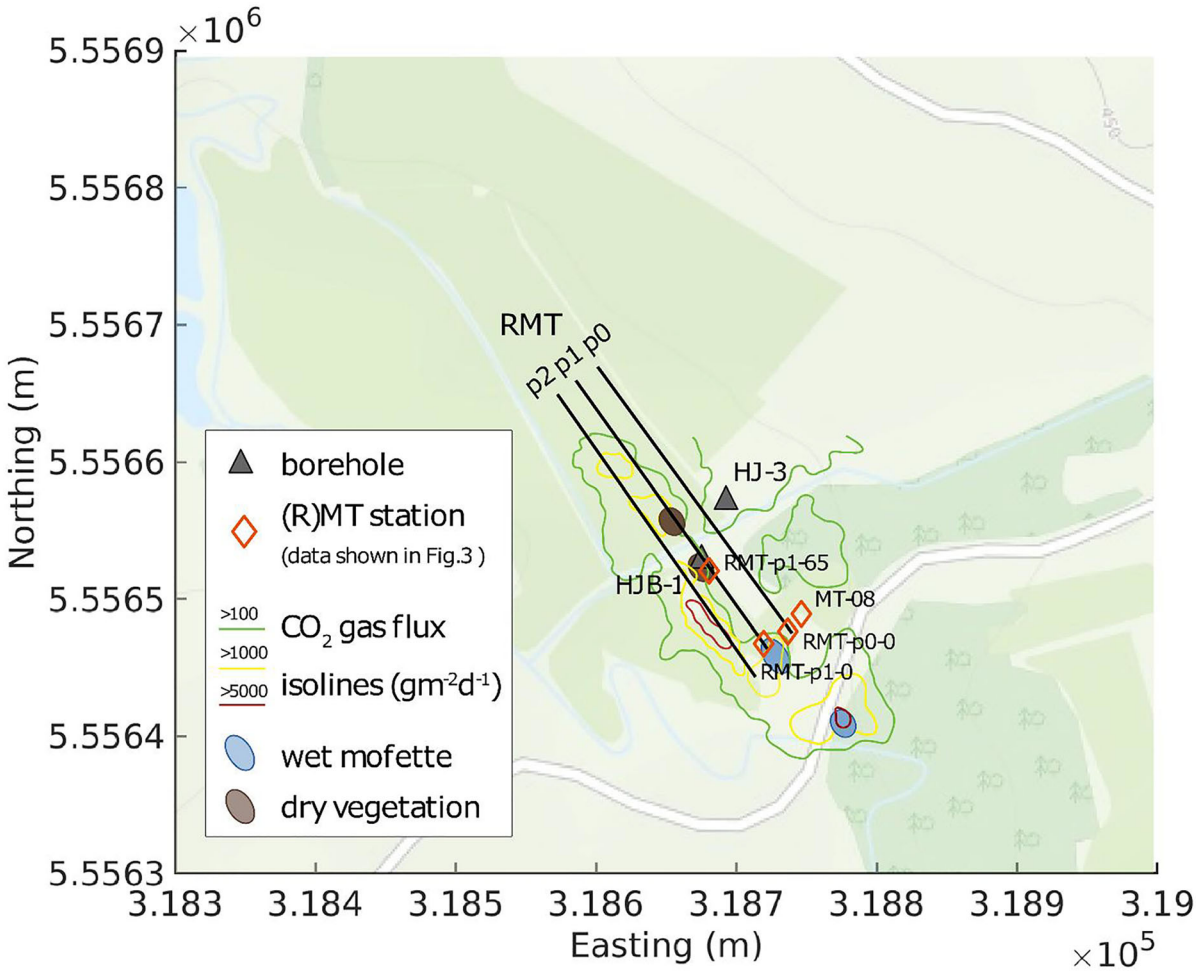

Figure 2
Map of the study area (HMF, indicated by the red rectangle in Fig. 1b) including RMT profiles and one MT station, mofette locations at the surface, two borehole locations (HJ-3 and HJB-1) and information on gas flux from Nickschick et al. (2015)

2001). The data were processed to estimate impedance tensor elements and VMTF in nine full-octave wide sub-bands with logarithmically equidistant target frequencies (see apparent resistivities and phases of three stations in Fig. 3 a-c). The number of the radio transmitters used was controlled by applying a signal-to-noise threshold of the horizontal magnetic field in which in this study was set to 10 dB, which is a common threshold for measurements with the EnviroMT system (Bastani et al., 2009, 2021). The field data processing schemes of the EnviroMT instrument are described in detail in Bastani (2001). The processing consists of the following four main steps: first, the number of radio

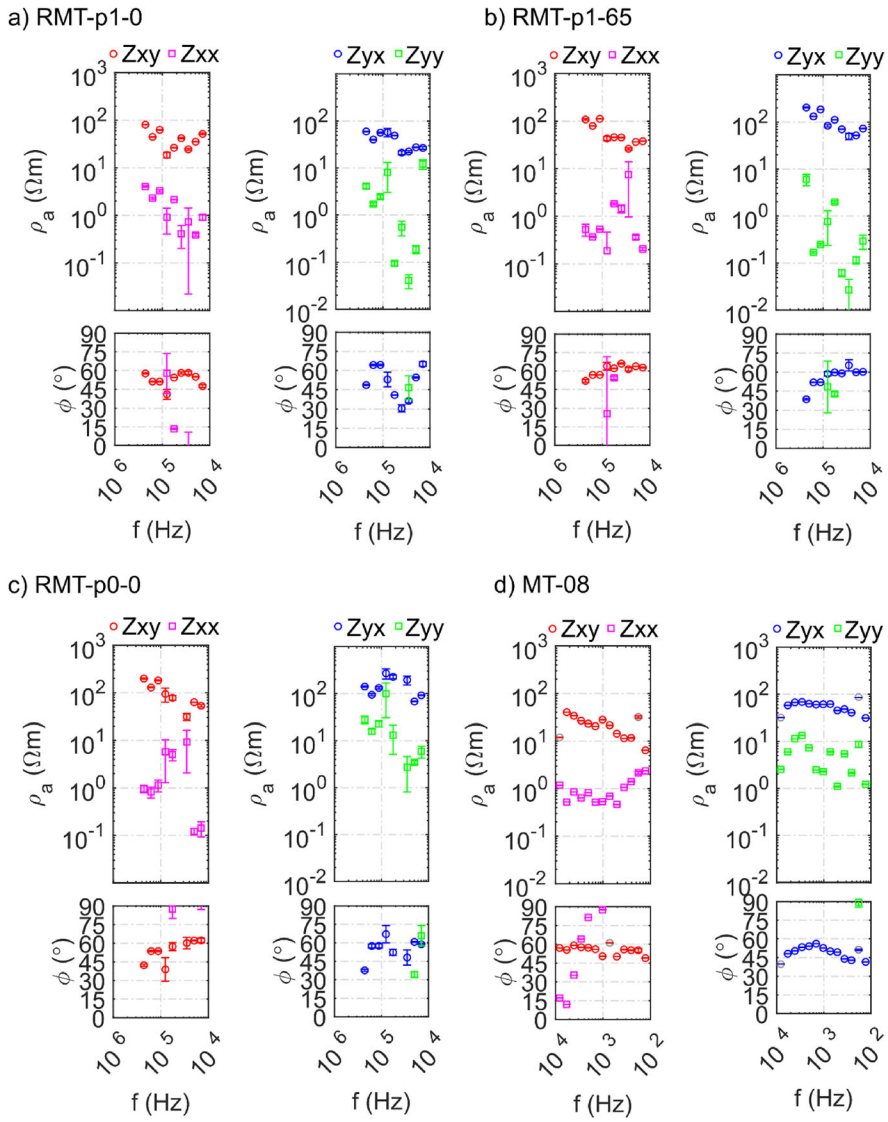

Figure 3

Original apparent resistivities and phases plotted over the measured frequency range of **a** the RMT station at 0 m distance (southernmost station) along RMT profile p1 at the location of the wet mofette, **b** the RMT station at 65 m distance along profile p1 at the location of the dry mofette next to borehole HJB-1, **c** the RMT station at 0 m distance along RMT profile p0 and **d** MT station MT-08 (cf. Fig. 2 for locations). High-frequency apparent resistivities of stations next to the wet mofettes as in **a** are decreased, and phases show higher variability compared to other stations. In the adjacent frequency bands, apparent resistivities of the MT station (**d**) and the neighbouring RMT station (**c**) are in the same range. Faded data points are possible outliers

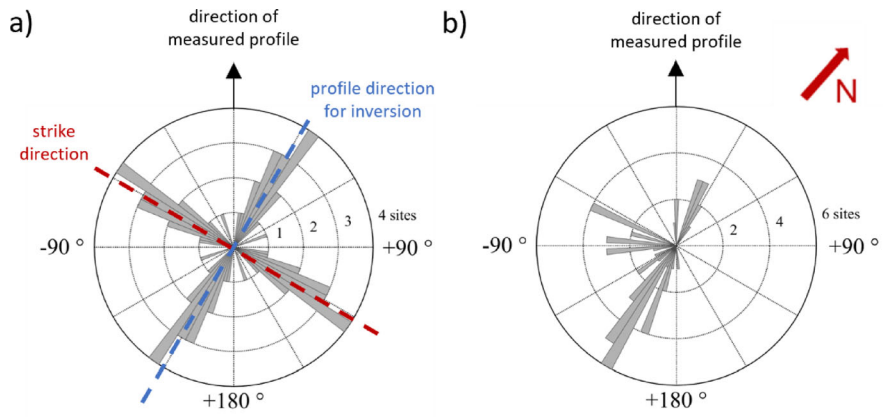

Figure 4

Rose diagrams showing the strike analysis of RMT profile p1 (cf. Fig. 2): **a** geoelectrical strike calculated excluding stations distorted by a power line, **b** corresponding induction vectors, modified after Rulff (2018). Induction vectors predominantly point SSW − 150° wrt. the measured profile direction, which indicates a geo-electric strike direction of − 60° wrt. the profile direction. To satisfy the assumption for 2D inversion that the regional resistivity distribution is two-dimensional and not varying in geo-electric strike direction, the profile direction for 2D inversion was rotated perpendicular to the geo-electric strike direction and the data coordinate system was rotated into the geoelectric strike direction. The stations were projected on the inversion profile, i.e. in the 2D inversions, the station spacing was smaller than in the field

transmitters is automatically selected according to the pre-defined signal-to-noise ratio. Second, auto and cross powers of the measured field components are mean stacked and stored at the selected transmitter frequencies. Third, the RMT transfer functions in each sub-band are estimated via the band-averaging method. As the radio transmitter frequencies are not evenly distributed over the recorded frequency range, a last postprocessing step developed by Bastani and Pedersen (2001) estimates the transfer functions to logarithmically equidistant target frequencies. This is done by an extended version of Weidelt's C function expansion (Weidelt & Kaikkonen, 1994) and a truncated singular value decomposition technique.

Transfer functions of a nearby MT station (location in Fig. 2) in a frequency range between 362 Hz and 8 kHz provided by Basel Aleid *(GFZ, pers. communication)* are shown in this study (Fig. 3d). They were processed using the EMRALD software package (Krings, 2007; Ritter et al., 1998; Weckmann et al., 2005). Comparing the apparent resistivities and phases at the MT station (Fig. 3d) and the neighbouring RMT station (Fig. 3c) in adjacent frequency bands, reveals them to lie in similar ranges. The apparent resistivities are 40–50 Ωm for the xy-component and 60–90 Ωm for the yx-component. The phases lie between 50 and 65°, while the xy-component is slightly higher than the yx-component for both, MT and RMT data. This shows that the RMT data are, despite of some noisy data points, of good quality even at the lower frequencies.

The practical depth of investigation (DOI) for EM data is dependent on the instrumental setup, the sensitivity and accuracy of the instrument, the resistivity distribution of the subsurface and the local noise level (Spies, 1989). The skin depth of inductive EM methods for a homogeneous half space in quasi-static approximation is defined as the depth, where the amplitude of the induced EM field is reduced to 1/e of the amplitude at the surface. According to Spies (1998), 1.5 skin depths are a rough estimate for the DOI of MT data. More accurate DOI calculations can be obtained via 1D inversion for a multi-layered earth, but they may be wrong in case static shift effects or 3D signatures are present in the data (Spies, 1989). We found that parts of our RMT data contain a relatively large amount of noise and the conductivity structure of the subsurface below the southern part of our measurement area is most likely three dimensional. Thus, we prefer to give a rough estimate for the DOI instead of presumably inaccurate values calculated for a 1D earth section. We decided to use one skin depth as a conservative estimate for the DOI of our recorded RMT data. Assuming an average resistivity of the subsurface between 75 and 100 Ωm

as indicated by an ERT resistivity model of the southern part of our measurement area (Flechsig et al., 2008), we derived a minimum skin depth between 9–10 m for the highest measured frequency of 250 kHz (cf. Fig. 9). However, since we are evaluating our RMT data in 2D and 3D, it is expected that shallower structures can also be resolved as the TM-mode is sensitive to currents generated by galvanic surface charges. The skin depth for the lowest measured frequency of 14 kHz lies between 37 and 43 m (cf. Fig. 9) giving a rough estimate for the maximum DOI of our RMT data.

Geoelectric strike and dimensionality of the RMT data were analysed using the ellipticity criterion introduced by Becken and Burkhardt (2004). The method is based on minimising ellipticities of the impedance tensor columns by rotating their coordinate system. If the minimal ellipticities are small, i.e. a clear geoelectric strike can be identified, an overall 2D subsurface conductivity distribution can be assumed. Five stations near electric lines show high EM noise levels resulting in biased results in the strike analyses. Subsequently, they were omitted during strike analyses, which revealed similar directions for all three measured profiles using the full frequency range of acquired data. Representative of the other profiles, the resulting rose diagrams of strike angle and induction vector distribution of profile p1 (23 stations, Fig. 4a, b) indicate, that the predominant geo-electric strike direction is − 60° with respect to the profile direction (corresponds to N80° E), as the main cluster of induction vectors points perpendicular to this direction. Note that strike analyses for separate frequencies unveiled, that data of the highest measured frequency (226 kHz) show higher variability in strike directions, such that near-surface 3D conductivity distributions might be assumed. Whereof the calculated geo-electric strike direction is caused, cannot be finally clarified. Large-scale geological structures such as the Ohře Graben, which strikes roughly with N55° E (Muñoz et al., 2018), are not assumed to be detected by the RMT signals.

Two scientific boreholes have been drilled in the measurement area (locations in Fig. 2) before our RMT measurements took place. Borehole HJ-3 (Sauer et al., 2014) provides stratigraphic information of the upper 15 m of the subsurface. In borehole HJB-1 (Bussert et al., 2017), comprehensive geochemical and geophysical investigations were performed starting at a depth of 15.5 m. We used the stratigraphic information, resistivity logs and observations about aquifer penetration and CO_2 outburst during the drilling for comparison with our RMT models. In borehole HJB-1, a laterolog system *(Thomas Wonik, Leibniz-Institut für Angewandte Geophysik (LIAG), pers. communication)*, sensitive to vertical and horizontal variations in resistivity, was used to measure apparent electrical resistivities every 5 cm. We applied the approach of averaging conductivities and resistivities of the laterolog measurements used in Pedersen et al. (1992) and Yan et al. (2017) to obtain average apparent resistivities for horizontally and vertically flowing currents, respectively. A comparison between the average apparent resistivities for horizontally and vertically flowing currents provides a convenient tool to investigate the presence of macro-scale anisotropy in the area. The apparent resistivities obtained with laterolog measurements in borehole HJB-1 are in a range between 2.7 and 22.0 Ωm. The calculated average apparent resistivities for horizontally and vertically flowing currents at 15.5–40 m depth are almost identical (Fig. 10), which justifies an isotropic inversion approach for the RMT data.

3.2. Inversion

We inverted our RMT data using two different inversion algorithms. 2D finite-difference RMT inversions were performed using *EMILIA* (Kalscheuer et al., 2008, 2010) on structured meshes. We ran an Occam inversion and a subsequent damped Occam inversion using the model with the lowest error from the Occam inversion as a start model. An Occam inversion is a Gauss–Newton based method, where the Lagrange multiplier is changed during each iteration, so that first the data misfit is minimised to a desired threshold and then the model is smoothed without increasing the data misfit again. In a damped Occam inversion, additional Marquardt–Levenberg damping is applied, which ensures only small model updates to enforce the inversion to converge. For 3D RMT inversions, the finite-difference based *ModEM* software package (Egbert & Kelbert, 2012; Kelbert

et al., 2014; Meqbel, 2009) was used. It inverts full impedance tensors using the non-linear conjugate gradient approach and structured grids.

To determine the resolution of our RMT data, we obtained model sensitivities (Fig. 11) using the approach to calculate scaled normalised accumulated sensitivities presented by Schwalenberg et al. (2002). The result is a sensitivity density distribution over the model domain and it shows to which degree individual model parameters are resolved by the entire data set. The analyses reveal that the highest sensitivities are between 0 and 25 m depth and that the sensitivities decrease strongly below this depth. We used the 10^{-3} sensitivity isolines to limit the interpretation ranges of the models because they correspond approximately to the estimated DOI.

General inversion settings:

The data fit is specified as the root-mean-squared fit: $RMS = \sqrt{\frac{1}{N}\sum_{n=1}^{N}\left(\frac{d_n^{obs}-d_n^{pred}}{\varepsilon_n}\right)^2}$, where N is the total number of datapoints and $\left(\frac{d_n^{obs}-d_n^{pred}}{\varepsilon_n}\right)$ describes the difference between the observed and predicted data weighted by their error floors. A homogeneous half space of 100 Ωm was used as an initial starting model if not specified otherwise. No topography had to be

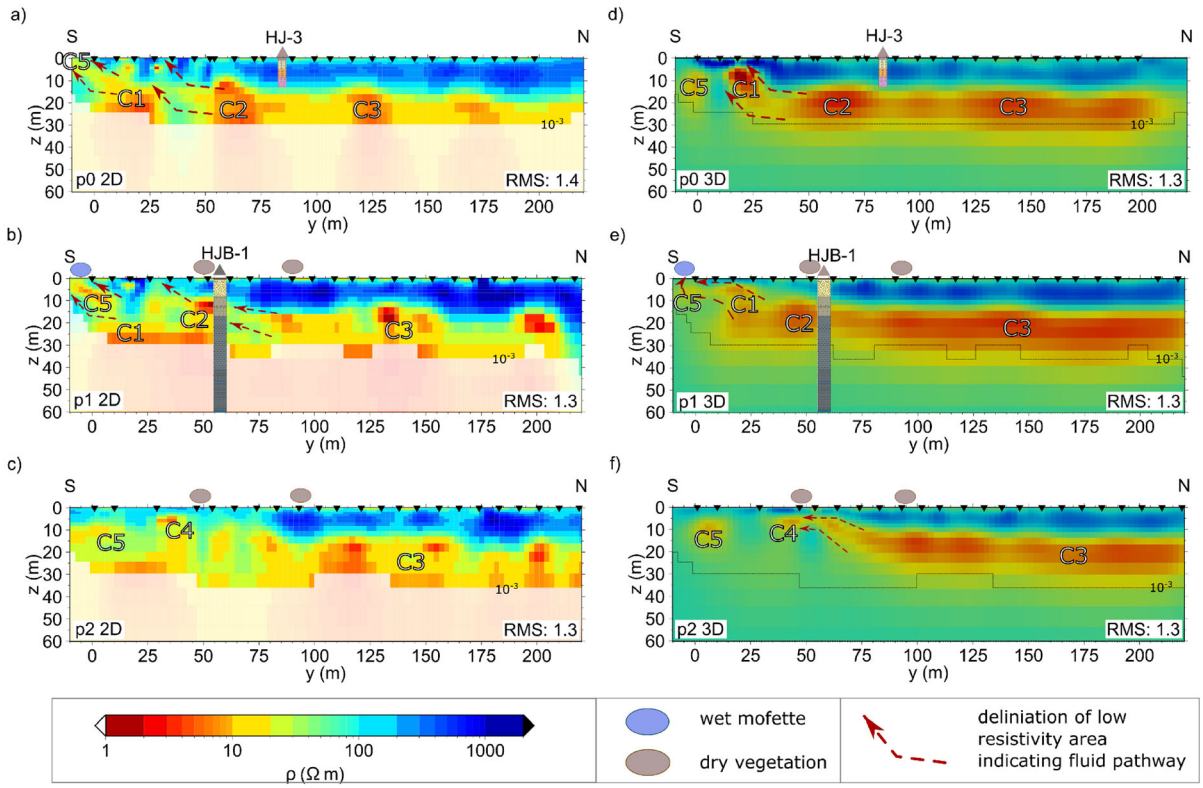

Figure 5

Inversion results of the RMT data (cf. Fig. 2 for profile locations). Black triangles mark RMT station locations. Prominent conductive anomalies are named with C1-C5. The colour scale is valid for all subfigures. The stratigraphies of boreholes HJB-1 and HJ-3 are displayed on top of the colour-coded resistivities (see Figs. 11, 15 for stratigraphy descriptions). **a**–**c** 2D models of RMT profiles p0, p1 and p2 obtained with Occam inversions and follow-up damped Occam inversions of RMT TE and TM mode data using EMILIA. Normalised sensitivities are shown in Fig. 10. The 10^{-3}-sensitivity isoline is used to fade out deeper model structures from interpretation. Station-wise RMS fits and pseudo-sections are shown in Figs. 12, 13, 14, 15. **d**, **e** Slices through the 3D RMT model obtained with ModEM along profiles p0, p1 and p2. For easier comparison with the 2D models, the slices are oriented along the computational profiles of the 2D inversion. Input data for the 3D inversion were impedance tensor elements. Station-wise RMS fits and pseudo-sections are shown in Figs. 16, 17, 18 and 19. The overall layered resistivity structure is predominantly disturbed in the southern part of the measurement area, where conductive anomalies C1, C4 and C5 are present close to the surface. They are connected to the deeper conductive anomalies C2 and C3 to the north. 2D and 3D models show similar features, but the centres of the anomalies and their connections are better distinguishable in the 3D model, which also appears to be smoother. The upper resistive layer correlates with sandy layers observed in the borehole stratigraphies

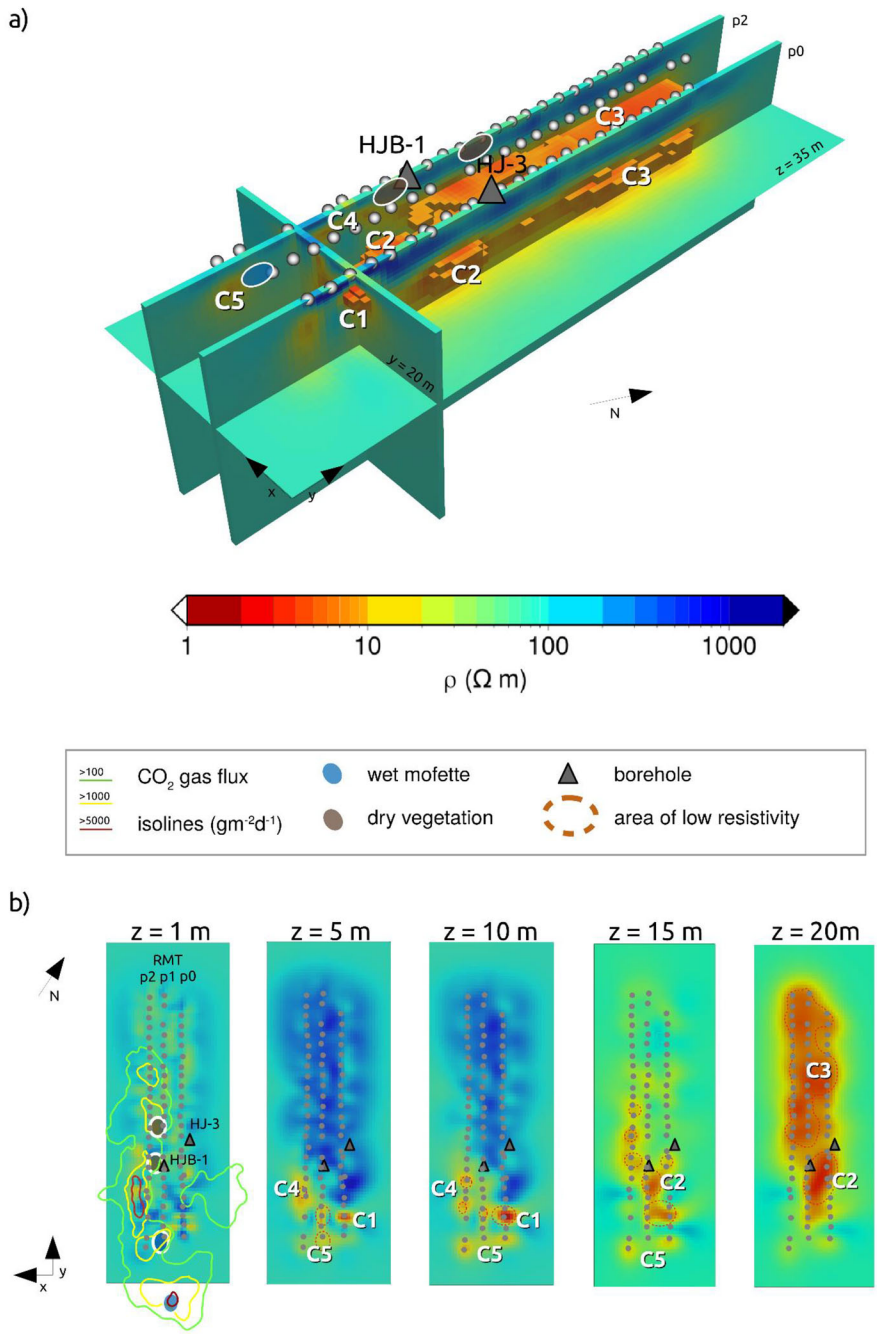

Figure 6

3D views of the 3D RMT model computed using ModEM. Grey dots mark the station locations. Prominent conductive anomalies are named with C1–C5. **a** Slices along profiles p0 and p2 and a perpendicular slice at the location of the conductive anomaly C1. Regions with resistivities below 10 Ωm are outlined. **b**) Depth slices of the 3D resistivity model. Information on surface gas flux from Nickschick et al. (2015) is plotted in the leftmost panel. Around the wet mofette in the south-eastern part of the 3D model, high gas flux correlates with decreased near-surface resistivities (C4, C5). Deeper prominent conductive anomalies (C1, C2, C3) are located beneath profiles p0 and p1 in reservoir-like features laterally offset to the location of the wet mofette expression at the surface. We interpret these conductive anomalies as fluid reservoirs connected to the mofettes at the surface

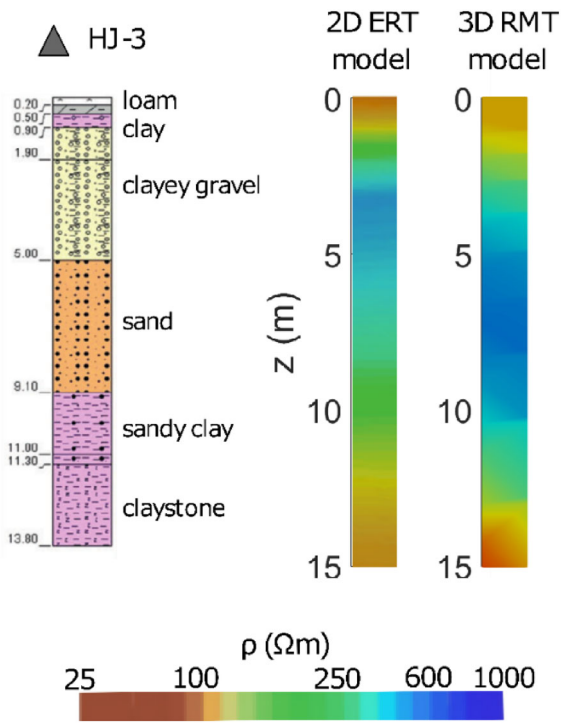

Figure 7
Comparison of RMT model and borehole data: Stratigraphy of borehole HJ-3 is compared to a vertical section of a 2D ERT model (modified after Sauer et al., 2014) closest to the borehole and to a vertical section of the 3D RMT model along the borehole in the same colour scale as the ERT model. The local resistivity distribution of the 3D RMT model fits the pattern of the ERT-derived resistivities. The clay and mudstone layers correlate with medium resistivities in our RMT model compared to higher resistivities in the sandy layer

considered for the inversion, because there are no significant elevation changes along and across the profiles. Displacement currents were neglected in all inversion approaches. As displacement currents can be present in resistive media at the measured RMT frequencies (cf. Fig. 9), we ran a test inversion with *EMILIA* accounting for displacement currents, but it had neither an influence on the model appearance nor on the RMS.

Model parameters were isotropic electrical resistivities. Only RMT impedance transfer functions served as input data for the inversions, because we investigated that the components of the vertical magnetic transfer function contain a relatively large amount of noise.

In the RMT inversions, vertical and horizontal smoothness constraints are weighted equally to also allow for vertical features, as we expect vertically and horizontally migrating fluids and horizontal layering. This choice is supported by tentative inversions using other combinations of smoothness constraints.

Error floors: To make the RMS misfits of all our models comparable, we choose 5% relative measurement error on the electric fields for all datasets if not specified otherwise. The error floors for the inverted quantities of the different methods result from applying the theory of Gaussian error propagation: We assume, that we only have measurement errors in the electric field. For the RMT data, 5% error on the electric field gives 5% relative error on the impedances, which corresponds to 10% relative error on the apparent resistivities and ca. 2.85° absolute error on the phases. In case the data error for a specific datapoint is larger than the specified error floor, the data error is used instead of the predefined error floor to down-weight the noisy data point in the inversion.

2D inversion Using apparent resistivities and phases of profiles p0, p1 and p2, a 2D TE and TM mode joint inversion was performed. To fulfil the assumption of a regional two-dimensional resistivity distribution of the subsurface which does not vary in geo-electric strike direction, the coordinate system was rotated into the direction of the determined geo-electric strike, so that the diagonal components of the impedance tensors get close to zero. Consequently, the input data for 2D inversion were those of the rotated coordinate system aligning the E_x and H_y components in the strike direction. Thus, the xy-components of the transfer functions represent the TE mode (electric field parallel to the geo-electric strike direction) and the yx-components represent the TM mode (electric field perpendicular to the geo-electric strike direction). Furthermore, the profile direction was rotated by + 30 and the station positions were projected on the profile in the rotated coordinate system.

Error floors on apparent resistivities were raised to 20% to account for static shift. The central model region was discretised with four cells between adjacent receivers and a vertical cell size of 0.5 m at the surface increasing by a factor of 1.2 towards depth. The overall model size including padding cells is 16 × 24 km. No prior reference model is used. For each profile, a standard Occam inversion of 25 iterations was conducted and the model with the

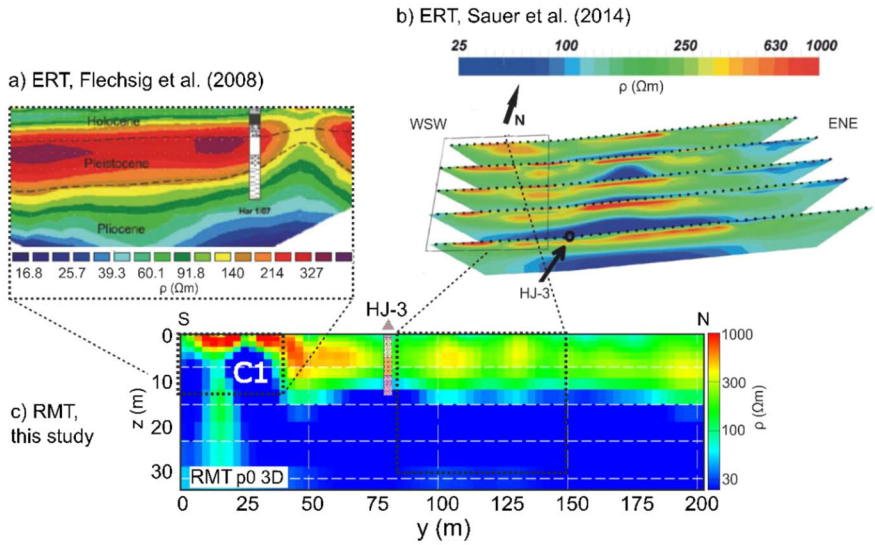

Figure 8
Comparison of extracts from ERT models (**a** Flechsig et al., 2008, **b** Sauer et al., 2014) and **c** the 3D RMT model along profile p0. Note that the colour scale of the RMT model is inverted and adjusted to be comparable to the ERT models' colour scales. Figure modified from Rulff (2018)

lowest RMS was subsequently used as a starting model for a damped Occam inversion.

3D inversion Input data for the 3D inversion were un-rotated impedance tensors of all RMT stations of profiles p0, p1, and p2. Whereas off-diagonal components of all stations were included, 50% of the diagonal components were neglected due to poor data quality. Consequently, error floors were raised to 20% for the absolute values of the remaining diagonal impedance tensor components. The central model domain was built with cells of 3 × 3 m horizontal size. Vertically, the thickness of the shallowest cells in the Earth is 0.5 m increasing by a factor of 1.2 down to 3 km depth. The overall model size is 0.64 × 0.64x3 km. The homogeneous half space starting model of 100 Ωm was also used as prior model. The inversion was run for 45 iterations.

4. Results

The 2D resistivity models (Fig. 5a–c) converged to RMS fits of 1.4, 1.3 and 1.3 for profiles p0, p1 and p2, respectively. The data fit tends to be better for the phases but is slightly worse in the southern part of profile p2 (Figs. 12, 13, 14, 15). The 2D models (Fig. 5a–c) show an overall disturbed layered structure: Distinct low resistivity anomalies (C1-C5, < 10 Ωm) appear in the shallow parts between 0 and 40 m profile distance and at greater depth farther north below a resistive (> 100 Ωm) upper layer.

The 3D inversion converged to an average RMS fit of 1.3. The data fit is better throughout the northern part of the model (Figs. 16, 17, 18, 19). In the 3D model (Figs. 5d, e, 6), anomalies appear with slightly lower contrasts than in the 2D models. The overall layered structure is clearly distinguishable: A 1–2 m thick cover layer of ca. 100 Ωm overlays a resistive layer of ca. 1000 Ωm, and a successive transition to resistivities less than 10 Ωm in the deeper parts can be observed. In the southern part of the model, the layered structure is disturbed by conductive anomalies (C1-C5, < 10 Ωm): The most conductive anomaly (C1, 1 Ωm in its centre) is located at a profile distance of 15–25 m and a depth of 5–16 m below profile p0, laterally extending towards profile p1. Less prominent conductive anomalies (C4 & C5) are located near the surface below profiles p1 and p2 and wider conductive regions (C2 & C3) at 15–30 m depth and 35–70 m profile distance in the whole model, whereas C2 is not present below profile p2.

In general, a decreasing trend in apparent electrical resistivity and impedance data with lower frequencies can be observed (Figs. 3, 13, 14, 15, 16, 17, 18, 19), which is reflected in our RMT models (Figs. 5, 6) as

well as in the apparent resistivities measured in borehole HJB-1 (Fig. 10, Bussert et al., 2017).

5. Discussion

5.1. Inversion approaches

We evaluated the measured RMT data using two different inversion algorithms in two and three dimensions. For the 2D inversion approach, apparent resistivity and phase data had to be rotated (Fig. 4) and some datapoints were excluded for the inversions (Figs. 13, 14, 15), as we identified them as outliers. However, these datapoints might as well been a hint for a 3D signature in the data. In the 3D inversion approach, all impedance tensor elements were included and no data rotation was performed. Thus, 3D information in the data was in principle not neglected. However, the diagonal impedance tensor elements are overall of smaller magnitude than the off-diagonal elements and thus more severely affected by noise. Even if therefore only a limited number of diagonal components could be used (Fig. 16), the 3D model is based on more data points, and thus more information in the subsurface, than the 2D models.

When comparing the 2D and 3D models (Fig. 5), they show similar features. However, it is noticeable that the centres of the conductive anomalies are located at slightly different locations. For example, one could deduce from the 2D RMT profile p1 (Fig. 5b) that the centres of anomalies C1 and C2 are located below profile p1, since the conductivity anomaly C1 has its largest extent and the anomaly C2 shows the highest conductivity values there. However, the 3D model (Figs. 5d–f, 6) indicates that the centre of the anomalies C1 and C2 might be rather located below profile p0. As the data of the two stations above the centre of the conductive anomaly C1 in the 3D model (stations 2, 3 profile p0 in Figs. 16, 17) are not well fitted, we cannot be entirely sure of the actual location of the anomaly centre. However, the data in the vicinity of anomaly C2 are better fitted by the 3D model than by the 2D model (stations 7–10 profile p0 in Figs. 16, 17), so that we can be certain that the centre of C2 is located below profile p0. C1 and C2 are, close to the surface, laterally connected to anomaly C5, which appears at the same location in the 3D and 2D models. The conductor C5 is located directly at the site of the wet mofette, which reinforces the interpretive approach of connected fluid reservoirs.

5.2. Integrated interpretation of resistivity models

To investigate whether the pathways of fluids and CO_2 in the shallow subsurface are detectable with the measured RMT data, we interpret the 2D and 3D resistivity models (Figs. 5, 6). All models show a locally interrupted layered structure fitting the near-surface stratigraphy of the sedimentary Cheb Basin observed in the boreholes (Figs. 5, 7, 10). The clay content of the sand layers decreases their resistivities as compared to units of pure sand.

The electrically conductive anomalies in the southern part of the profiles (C1, C2, C4 & C5 in Figs. 5 and 6) in the vicinity of the wet mofette at the surface (cf. Figs. 2 and 6b leftmost panel) can be interpreted as local reservoirs and fluid pathways of a few metres in diameter, where the pore spaces of the soil layers and bedrock are filled with mineral water containing CO_2 - rich gases. However, only the 3D model reveals, that the centre of the two conductive reservoirs connected to the wet mofette are not directly below it but shifted towards the East at a depth of 6–16 m (C1) and further down towards the North (C2) at a depth of 15–24 m (Figs. 5d, e, 6). The location of the latter conductive anomaly (C2) corresponds to the location of borehole HJB-1 (panels 4 and 5 in Fig. 6b). There, we discern a dry mofette at the surface, medium resistivities in the upper 10 m, but the aforesaid conductive anomaly at greater depth. Observations during the drilling of HJB-1 (Bussert et al., 2017) help to interpret and extrapolate our models: Whereas a very shallow aquifer at 0.6 m below the surface does not correspond to a distinct increased near-surface conductivity in the 3D model, we can see locally low resistivity (10 Ωm) in the upper cells next to the borehole location in the 2D model of profile p1 (Fig. 5b). Furthermore, we can directly correlate the conductive anomaly at about 20 m depth (C2) observed in our RMT models with an aquifer reached during drilling at the same depth (Fig. 10). Additionally, at ca. 80 m depth, an aquifer was hit containing sub-thermal mineral water with resistivities of 1.5 Ωm. The depth of this aquifer cannot be resolved by our RMT data, but MT models presented by Platz et al. (2022) indicate high

conductivities down to 80 m depth below the mofette field. Combining the mofette locations at the surface, the resistivity distribution of the RMT models and the borehole data of HJB-1 leads to the conclusion that one or more fluid reservoirs are located at the borehole location at 0.6–80 m depth. Our models suggest that these reservoirs are connected to the mofettes at the surface. Whereas a water-CO_2 mixture reaches the surface at the wet mofette, only the gaseous CO_2, which might not exhibit a strong resistivity contrast to the sandy basin layers, migrates up to the surface at the dry mofette above the reservoir.

Probably, the less prominent conductive anomalies in the central and northern parts of the RMT profiles (Figs. 5, 6) are also related to fluid reservoirs. However, mofette structures and increased gas flux at the surface are only observed for the central, but not the northern parts of the profiles, where the conductive anomalies could also be caused by increased clay content.

The RMT models obtained in this study compare well to the resistivity models covering parts of our study area that were derived from ERT data in recent years. In the southern part of the study area, an upwelling conductive area in the ERT model of Flechsig et al. (2008) corresponds to the location of the conductive anomaly C1 in the RMT model below profile p0 (Fig. 8a, c). The conductive anomaly is more prominent in the RMT model than in the ERT model. In the middle part, the more resistive cover layer in the RMT models is verified by resistivity models derived from ERT data measured by Sauer et al. (2014) along perpendicular profiles (Fig. 8b, c). At the borehole location of HJ-3, the local resistivity distribution of the 3D RMT model fits the pattern of the ERT-derived resistivities (Fig. 7).

The RMT models contribute with a detailed image of the near-surface aquifer structures in the HMF. While large-scale conceptual models of e.g. Nickschick et al. (2019) appraise a near vertical upwelling and diffusion of CO_2 along the major fault PPZ crossing the HMF, our models additionally infer a reservoir-and-channel structure for the upper 35 m before the CO_2 reaches the surface either in combination with or without water. The conductive reservoir centres are not necessarily located directly vertically below the mofettes indicating that fluids are moving in horizontal and vertical directions within the mofette fields. MT models (Mair, 2020; Muñoz et al., 2018; Platz et al., 2022) suggest that these structures continue at greater and that the reservoirs are most likely located laterally offset to the mofette locations at the surface.

6. Conclusion

The mofette fields in the Cheb basin have been studied with a variety of methods in recent years. The presented resistivity models obtained with RMT data confirm and supplement the current interpretation of the near-surface migration of CO_2-bearing fluids. We identified the RMT technique as a useful tool to further constrain the detailed fluid pathways imaged as highly conductive anomalies in the resistivity models. In general, we recommend a 3D evaluation to be able to locate the near-surface reservoir features correctly and avoid false projection onto 2D models.

Author Contributions All authors contributed to the study conception and design. P.R., U.W., L.B. and G.W. conducted the measurements. P.R., A.P. and U.W. processed the data. P.R. and T.K. performed the inversions. The first draft of the manuscript was written by P.R. and all authors commented on previous versions of the manuscript. All authors contributed to, read and approved the final manuscript.

Funding

Open access funding provided by Uppsala University. We thank GFZ Potsdam for funding the measurements. We appreciate the availability of MT data recorded with MT instruments from the Geophysical Instrument Pool Potsdam.

Data Availability

The radio-magnetotelluric data, that were collected for this work and support the findings of this study, are available from the corresponding author upon reasonable request.

Declarations

Conflict of interest The authors have no conflict of interest, financial or otherwise.

Appendix

See Additional Figs. 9, 10, 11, 12, 13, 14, 15, 16, 17, 18, and 19

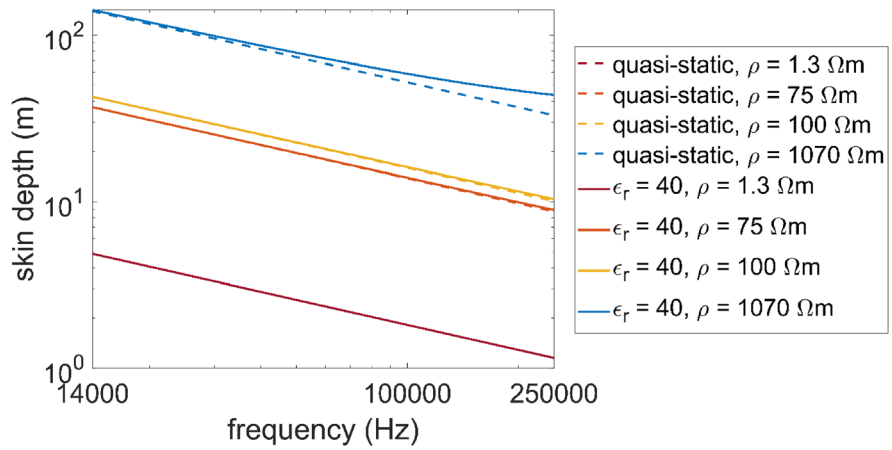

Fig. 9

Skin depths for a minimum half space resistivity of 1.3 Ωm, two medium resistivities of 75 and 100 Ωm, and a maximum resistivity of 1070 Ωm plotted over the measured RMT frequency range. The resistivities were derived from a resistivity model of the southern part of our measurement area which was created with ERT data (Flechsig et al., 2008). The skin depths are plotted for the quasi-static case ($\varepsilon_r = 0$) and for a case, where displacement currents were considered ($\varepsilon_r = 40$). The skin depth is altered by displacement currents only in the maximum resistivity scenario at the highest frequencies

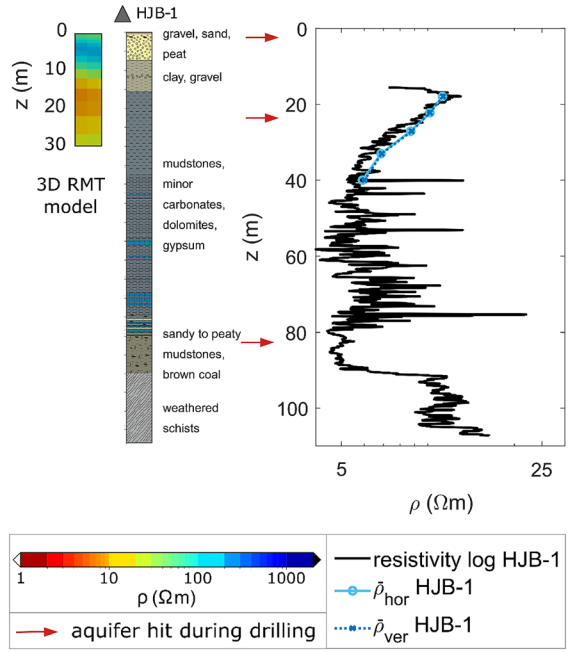

Fig. 10

Stratigraphy and apparent resistivities of laterolog measurements in borehole HJB-1 with depth of penetrated aquifers (modified after Bussert et al., 2017) and average apparent resistivities (ρ_{hor}, ρ_{ver}) of HJB-1 for horizontally and vertically flowing currents obtained by averaging the laterolog data (following Pedersen et al., 1992). As ρ_{hor} and ρ_{ver} are approximately the same, an isotropic inversion approach is justified. The location of an aquifer and a minimum in resistivity in borehole HJB-1 at approx. 20 m depth match the conductive anomaly in the 3D model at the borehole location (cf. C2 in Figs. 4, 5). Note, that the resistivities obtained with focused electrical resistivity measurements in the borehole HJB-1 cannot be directly correlated to the resistivity models obtained with RMT data due to the different measurement methods and their resolution scales. However, a comparison of the upper 30 m of the 3D RMT model at the borehole location to the stratigraphy indicates a correlation of the sandy top layer and the clays and mudstones below with high and low resistivities in the model, respectively

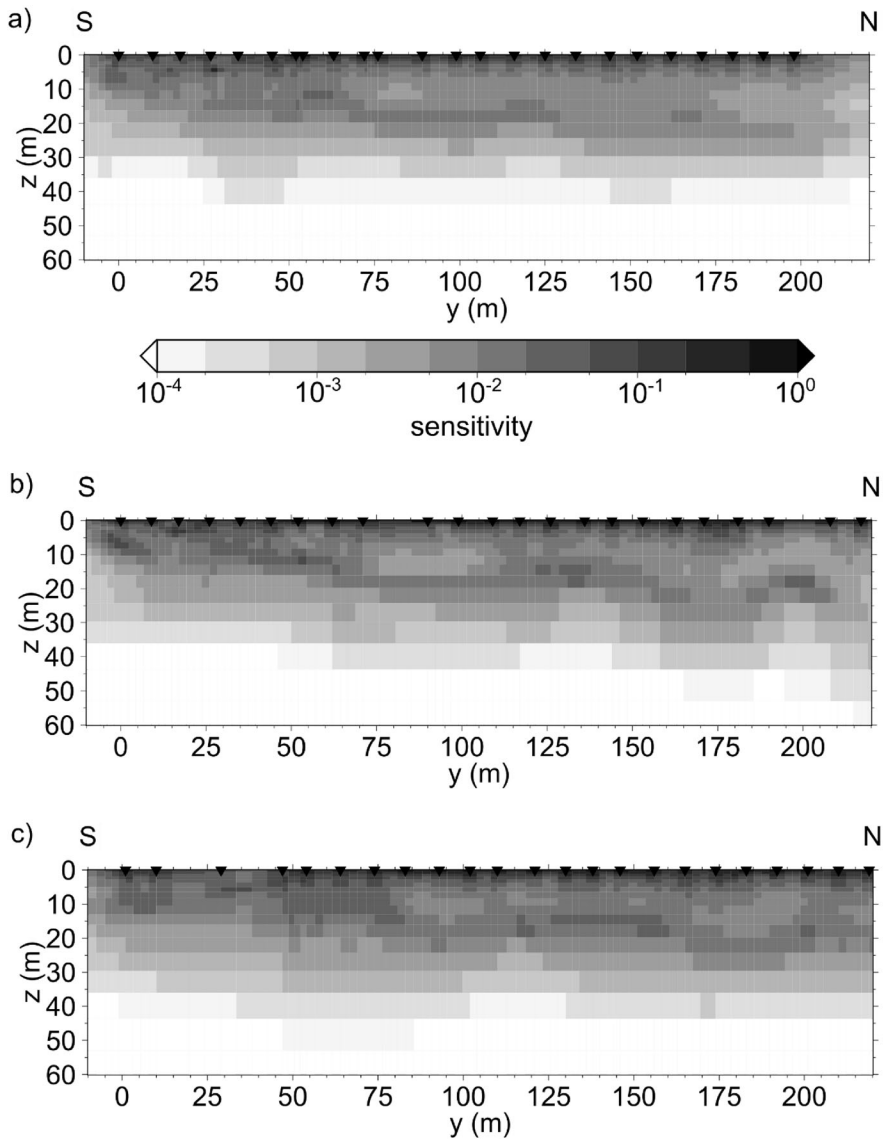

Fig. 11
Normalised accumulated sensitivities of the 2D models (Fig. 5a–c) using the approach of Schwalenberg et al., 2002. The subfigures **a**, **b** and **c** correspond to profiles p0, p1, p2, respectively

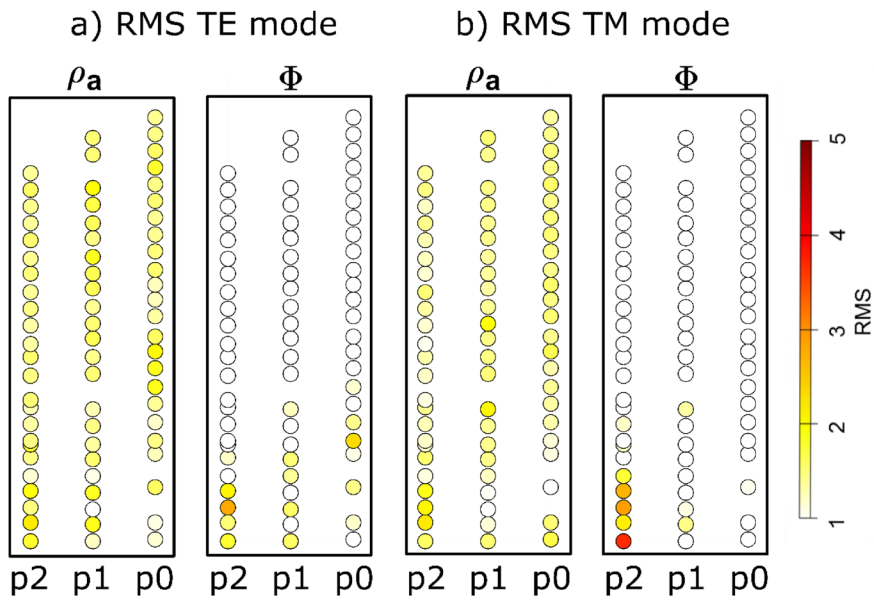

Fig. 12
RMS distribution in TE mode (**a**) and TM mode (**b**) averaged over frequency for all stations included in the 2D inversions. Overall, the RMS fit for phases is better than for apparent resistivities

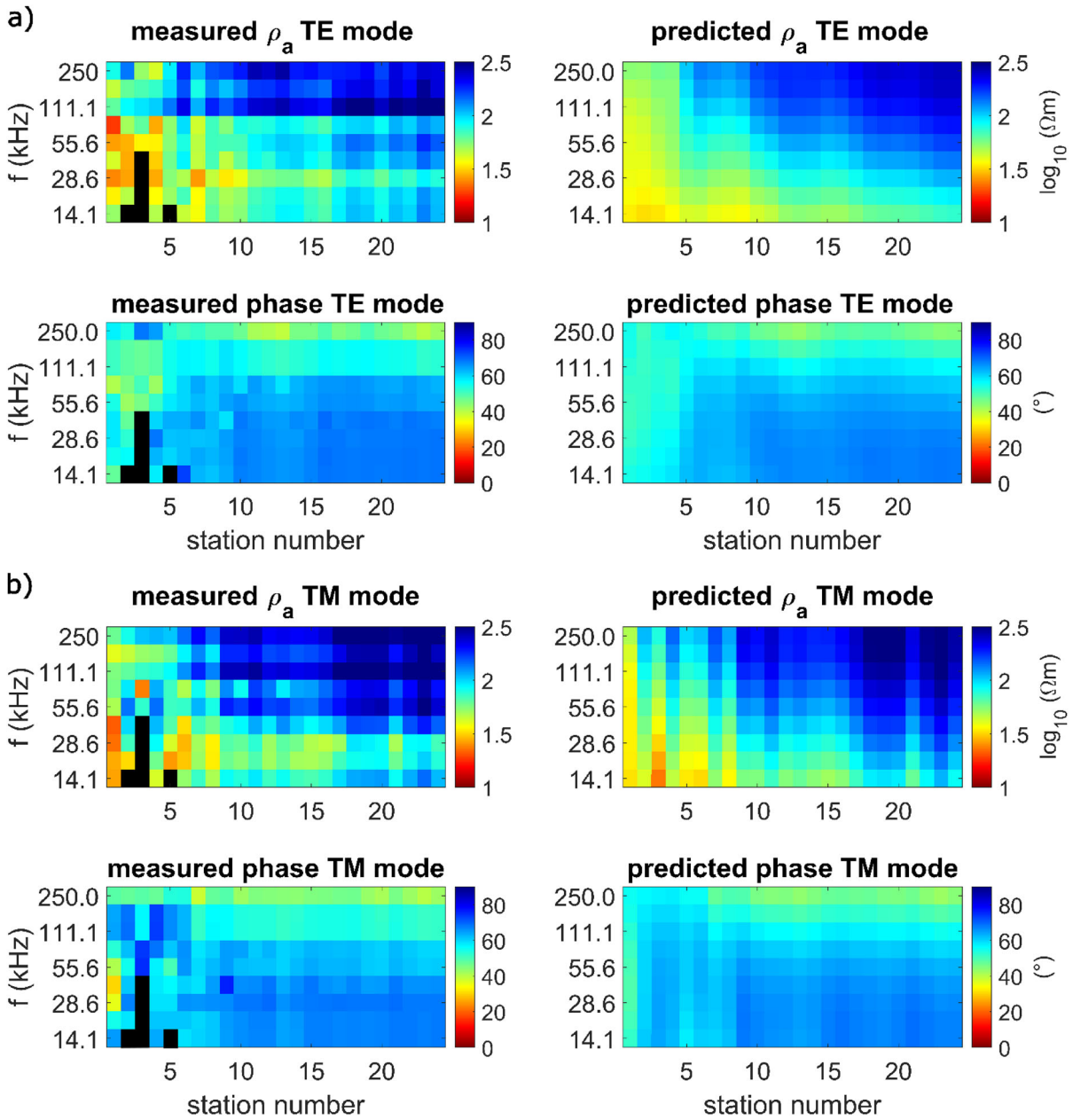

Fig. 13
Pseudo-sections of profile p0 for **a** TE mode and **b** TM mode of rotated measured and predicted data. Black colour marks single data points excluded from the 2D inversion

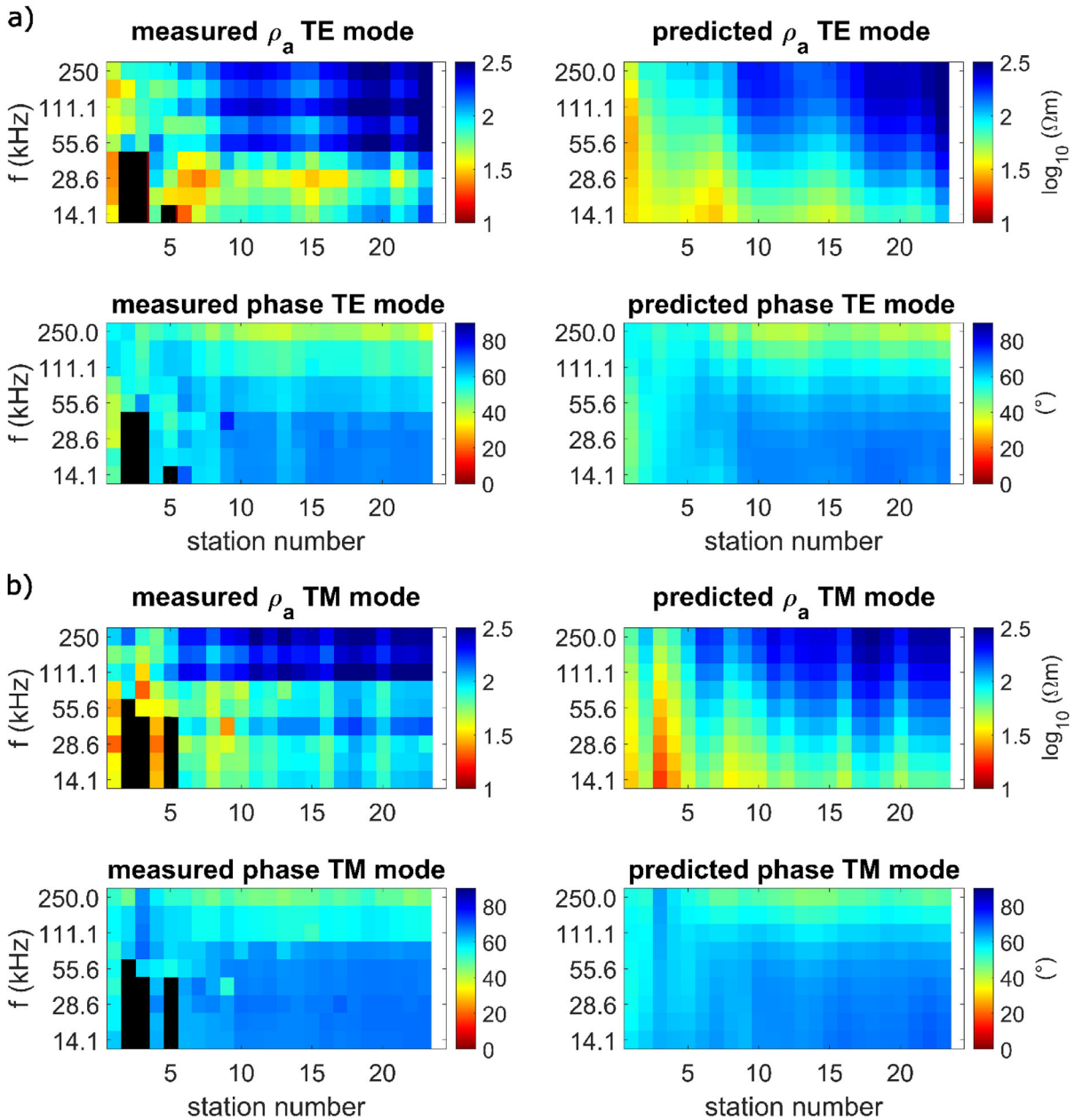

Fig. 14
Pseudo-sections of profile p1 **a** TE mode and **b** TM mode of rotated measured and predicted data. Black colour marks single data points excluded from the 2D inversion

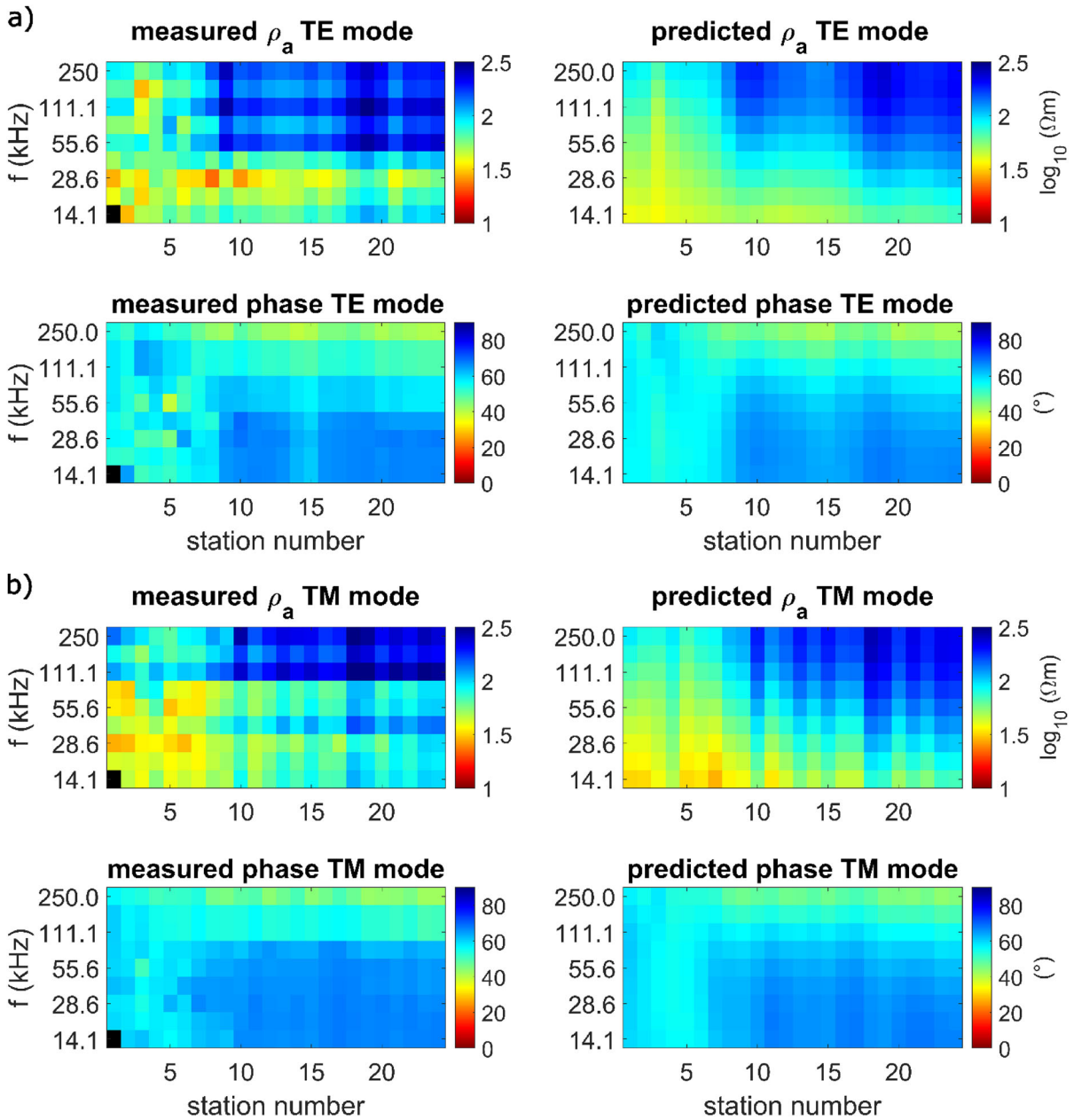

Fig. 15
Pseudo-sections of profile p2 for **a** TE mode and **b** TM mode of rotated measured and predicted data. Black colour marks single data points excluded from the 2D inversion

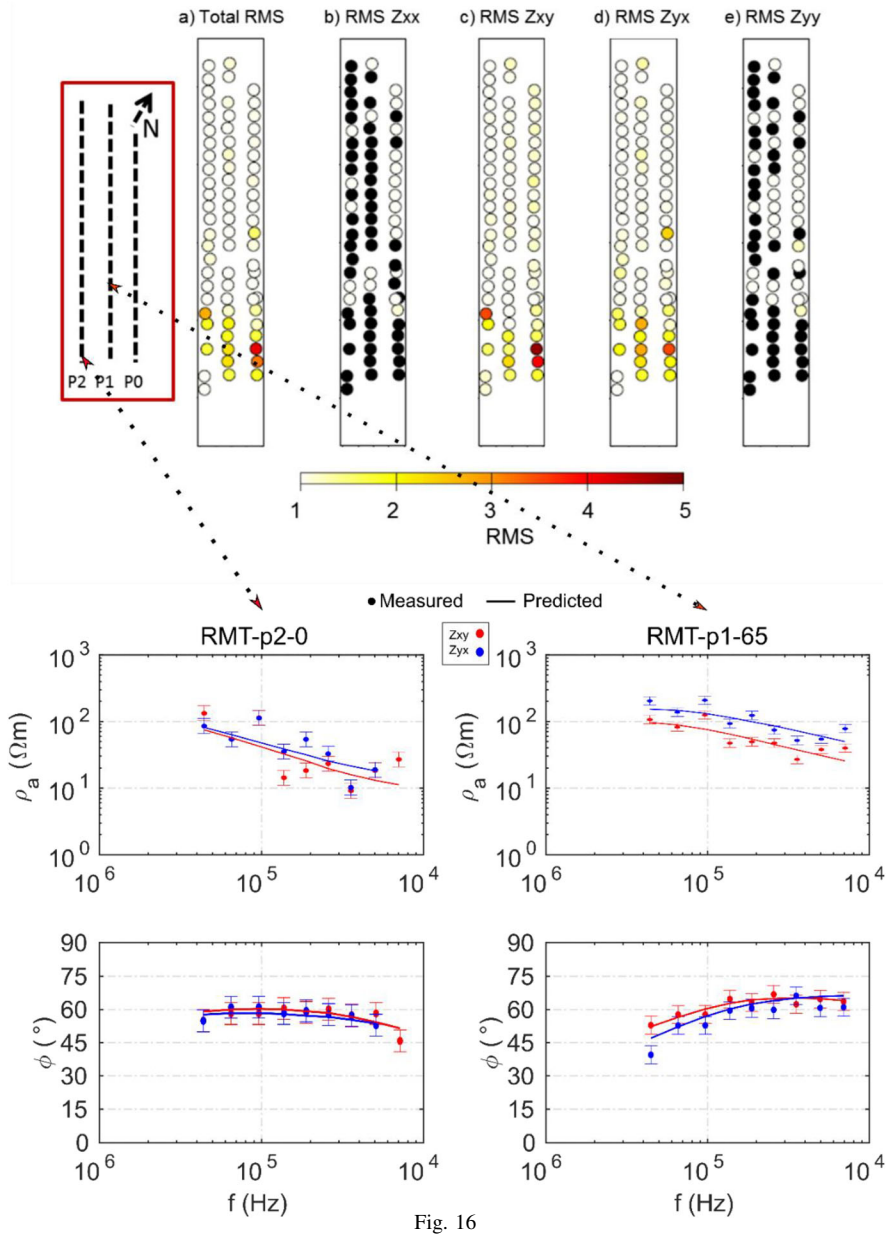

Fig. 16

RMS distribution averaged over frequency and components (**a**) and for individual impedance tensor components (**b**–**e**) for each station included in the 3D inversion and exemplary data fit plots for two stations (below). Black dots mark components excluded from the inversion because of poor data quality. Overall, the data fit in the northern part of the model is better. Figure modified after Rulff (2018)

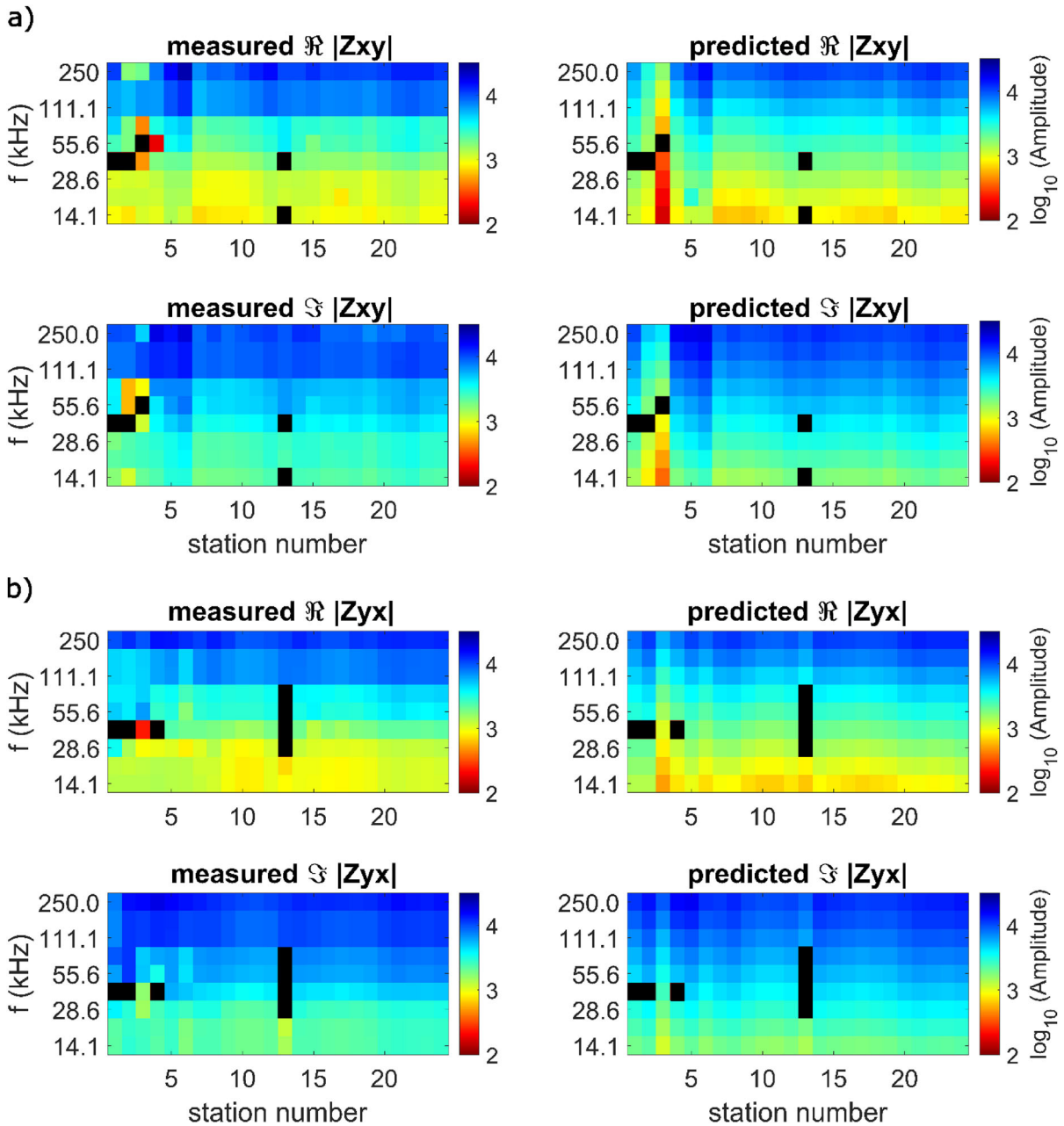

Fig. 17
Pseudo-sections of profile p0 for **a** Zxy and **b** Zyx components of measured and predicted data. Black colour marks single data points excluded from the 3D inversion because of poor data quality

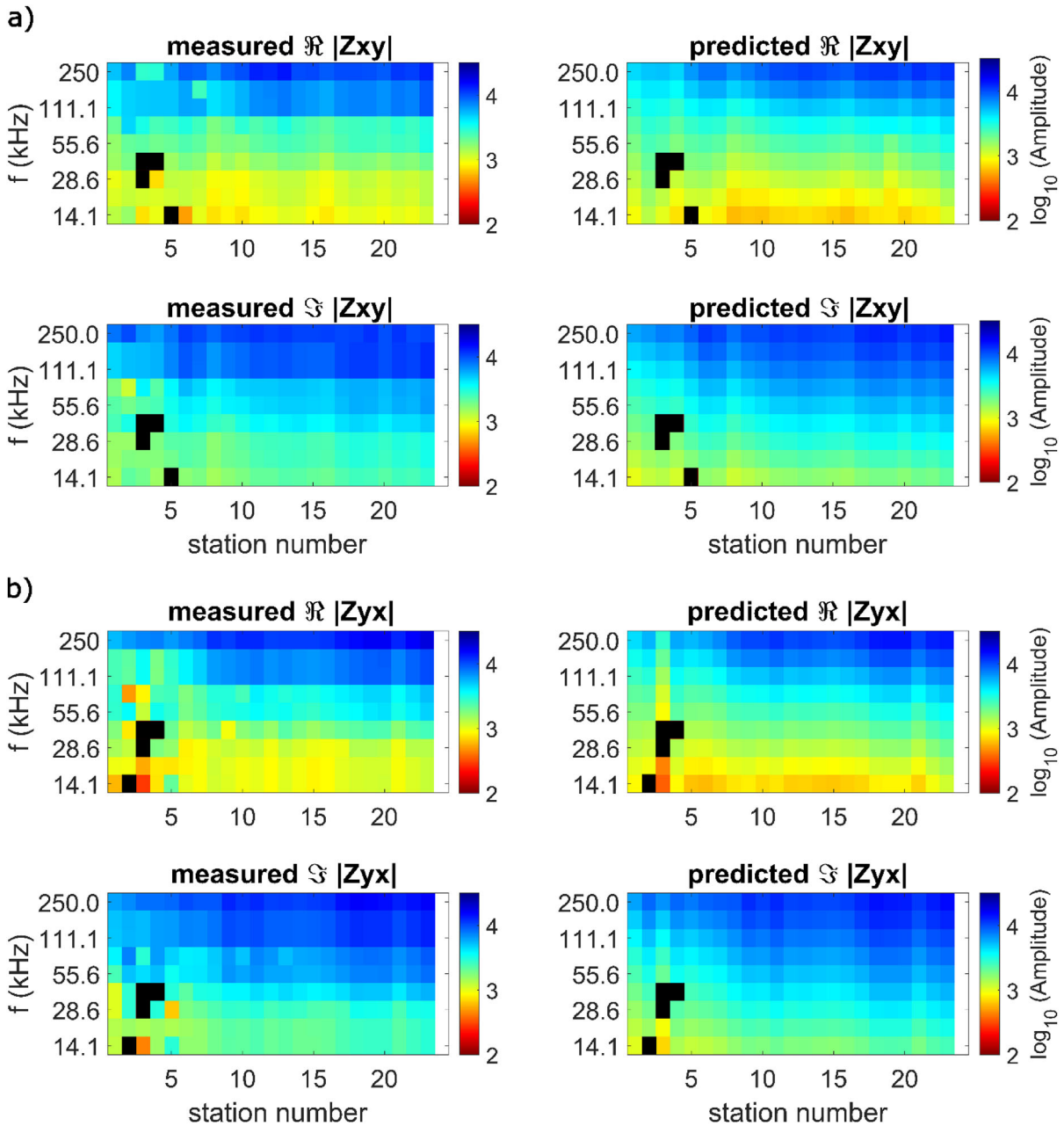

Fig. 18
Pseudo-sections of profile p1 for **a** Zxy and **b** Zyx components of measured and predicted data. Black colour marks single data points excluded from the 3D inversion because of poor data quality

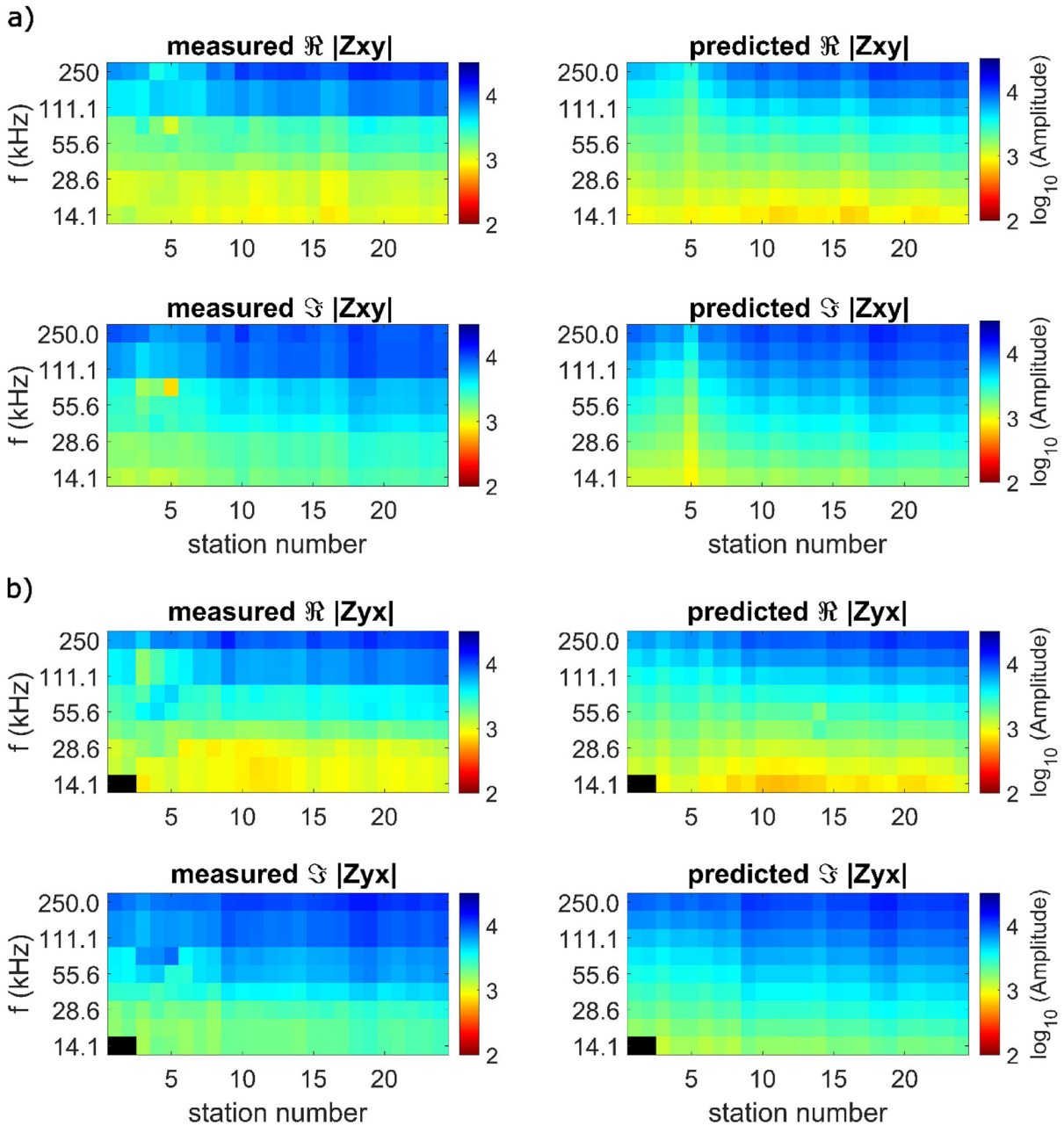

Fig. 19
Pseudo-sections of profile p2 for **a** Zxy and **b** Zyx components of measured and predicted data. Black colour marks single data points excluded from the 3D inversion because of poor data quality

References

Aleid, B., Weckmann, U. Platz, A., Pek, J., Kováčiková, S., & Klanica, R. (2022). 3D imaging of electrical conductivity structures in the Eastern Cheb Basin across the Hartoušov and Bublák mofettes. In 25th EMIW induction workshop, Türkiye.

Bankwitz, P., Schneider, G., Kämpf, H., & Bankwitz, E. (2003). Structural characteristics of epicentral areas in Central Europe: Study case Cheb Basin (Czech Republic). *Journal of Geodynamics, 35*, 5–32.

Bastani, M. (2001). EnviroMT—A new controlled source/radio magnetotelluric system. PhD thesis, Uppsala University.

Bastani, M., Malehmir, A., Ismail, N., Pedersen, L. B., & Hedjazi, F. (2009). Delineating hydrothermal stockwork copper deposits using controlled-source and radio-magnetotelluric methods: A case study from northeast Iran. *Geophysics*. https://doi.org/10.1190/1.3174394

Bastani, M., & Pedersen, L. B. (2001). Estimation of magnetotelluric transfer functions from radio transmitters. *Geophysics, 66*(4), 1038–1051. https://doi.org/10.1190/1.1487051

Bastani, M., Wang, S., Malehmir, A., & Mehta, S. (2021). Radio-magnetotelluric and controlled-source magnetotelluric surveys on a frozen lake: Opportunities for urban applications in Nordic countries. *Near-Surface Geophysics*. https://doi.org/10.1002/nsg.12180

Becken, M., & Burkhardt, H. (2004). An ellipticity criterion in magnetotelluric tensor analysis. *Geophysical Journal International, 159*, 69–82.

Bräuer, K., Kämpf, H., Niedermann, S., Strauch, G., & Tesař, J. (2008). Natural laboratory NW Bohemia: Comprehensive fluid studies between 1992 and 2005 used to trace geodynamic processes. *Geochemistry, Geophysics, Geosystems, 9*(4), Q04018. https://doi.org/10.1029/2007GC001921

Bräuer, K., Kämpf, H., & Strauch, G. (2009). Earthquake swarms in non-volcanic regions: What fluids have to say. *Geophysical Research Letters, 36*, 1–5. https://doi.org/10.1029/2009GL039615

Bräuer, K., Kämpf, H., & Strauch, G. (2014). Seismically triggered anomalies in the isotope signatures of mantle-derived gases detected at degassing sites along two neighboring faults in NW Bohemia, central Europe: Seismically induced anomalies. *Journal of Geophysical Research: Solid Earth*. https://doi.org/10.1002/2014JB011044

Bussert, R., Kämpf, H., Flechsig, C., Hesse, K., Nickschick, T., Liu, Q., Umlauft, J., et al. (2017). Drilling into an active mofette: Pilot-hole study of the impact of CO_2-rich mantle-derived fluids on the geo-bio interaction in the western Eger Rift (Czech Republic). *Scientific Drilling, 23*, 13–27. https://doi.org/10.5194/sd-23-13-2017

Daskalopoulou, K., Woith, H., Zimmer, M., Niedermann, S., Barth, J. A. C., Frank, A. H., Vieth-Hillebrand, A., et al. (2021). Insight into Hartoušov Mofette, Czech Republic: Tales by the fluids. *Frontiers of Earth Science*. https://doi.org/10.3389/feart.2021.615766

Egbert, G. D., & Kelbert, A. (2012). Computational recipes for electromagnetic inverse problems. *Geophysical Journal International, 189*, 251–267. https://doi.org/10.1111/j.1365-246X.2011.05347.x

Fischer, T., Horálek, J., Hrubcová, P., Vavryčuk, V., Bräuer, K., & Kämpf, H. (2014). Intra-continental earthquake swarms in West-Bohemia and Vogtland: A review. *Tectonophysics, 611*, 1–27. https://doi.org/10.1016/j.tecto.2013.11.001

Fischer, T., Hrubcová, P., Dahm, T., Woith, H., Vylita, T., Ohrnberger, M., Vlček, J., et al. (2022). ICDP drilling of the Eger Rift observatory: Magmatic fluids driving the earthquake swarms and deep biosphere. *Scientific Drilling, 31*, 31–49. https://doi.org/10.5194/sd-31-31-2022

Flechsig, C., Bussert, R., & Rechner, J. (2008). The Hartousov mofette field in the Cheb Basin, Western Eger Rift (Czech Republic): A comperative geoelectric, sedimentologic and soil gas study of a magmatic diffuse CO_2-degassing structure. *Zeitschrift Für Geologische Wissenschaften, 36*, 177–193.

Flores Estrella, H., Umlauft, J., Schmidt, A., & Korn, M. (2016). Locating mofettes using seismic noise records from small dense arrays and matched field processing analysis in the NW Bohemia/Vogtland Region, Czech Republic. *Near Surface Geophysics, 14*, 327–337. https://doi.org/10.3997/1873-0604.2016024

Geissler, W. H., Kämpf, H., Kind, R., Bräuer, K., Klinge, K., Plenefisch, T., Horalek, J., Zednik, J., & Nehybka, V. (2005). Seismic structure and location of a CO_2 source in the upper mantle of the western Eger (Ohre) Rift, central Europe. *Tectonics, 24*, TC5001.

Horálek, J., & Fischer, T. (2008). Role of crustal fluids in triggering the West Bohemia/Vogtland earthquake swarms: Just what we know (a review). *Studia Geophysica Et Geodaetica, 52*, 455–478.

Kalscheuer, T., de Los Ángeles García Juanatey, M., Meqbel, N., & Pedersen, L. B. (2010). Non-linear model error and resolution properties from two-dimensional single and joint inversions of direct current resistivity and radiomagnetotelluric data. *Geophysical Journal International, 182*, 1174–1188. https://doi.org/10.1111/j.1365-246X.2010.04686.x

Kalscheuer, T., Pedersen, L. B., & Siripunvaraporn, W. (2008). Radiomagnetotelluric two-dimensional forward and inverse modelling accounting for displacement currents. *Geophysical Journal International, 175*, 486–514. https://doi.org/10.1111/j.1365-246X.2008.03902.x

Kämpf, H., Broge, A. S., Marzban, P., Allahbakhshi, M., & Nickschick, T. (2019). Nonvolcanic carbon dioxide emission at continental rifts: The Bublak Mofette Area, Western Eger Rift, Czech Republic. *Geofluids*. https://doi.org/10.1155/2019/4852706

Kämpf, H., Geissler, W.H. & Bräuer, K. (2007) Combined gas-geochemical and receiver function studies of the Vogtland/NW Bohemia Intraplate Mantle Degassing Field, Central Europe. Ritter, J.R.R. Christ. U.R. Mantle Plumes—A multi-disciplinary approach., 127–158.

Kelbert, A., Meqbel, N., Egbert, G. D., & Tandon, K. (2014). ModEM: A modular system for inversion of electromagnetic geophysical data. *Computers & Geosciences, 66*, 40–53. https://doi.org/10.1016/j.cageo.2014.01.010

Kraft, P., Linnemann, U., Mergl, M., Bruthansová, J., Laibl, L., & Geyer, G. (2023). Ordovician of the Bohemian Massif. *Geological Society, London, Special Publications, 532*, 433–464. https://doi.org/10.1144/sp532-2022-191

Krings, T. (2007). The influence of robust statistics, remote reference, and horizontal magnetic transfer functions on data processing in magnetotel- lurics. Master's thesis, Institut fur Geophysik Westfalische Wilhelms- Universitat Munster and GeoForschungsZentrum Potsdam.

Mair, J. (2020). Interpretation of MT Data in the Eger Rift along the Regional Profiles. Master thesis. Freie Universität Berlin, Berlin.

Matte, P., Maluski, H., Rajlich, P., & Franke, W. (1990). Terrane boundaries in the Bohemian Massif: Result of large-scale Variscan shearing. *Tectonophysics, 177*, 151–170.

Matys Grygar, T., Elznicová, J., Kiss, T., & Smith, H. G. (2016). Using sedimentary archives to reconstruct pollution history and sediment provenance: The Ohře River, Czech Republic. *CATENA, 144*, 109–129. https://doi.org/10.1016/j.catena.2016.05.004

Meqbel, N. (2009). *The electrical conductivity structure of the Dead Sea Basin derived from 2D and 3D inversion of magnetotelluric data*. Freie Universität Berlin.

Mrlina, J., Kämpf, H., Kroner, C., Mingram, J., Stebich, M., Brauer, A., Geissler, W., Kallmeyer, J., Matthes, H., & Seidl, M. (2009). Discovery of the first Quaternary maar in the Bohemian Massif, Central Europe, based on combined geophysical and geological surveys. *Journal of Volcanology and Geothermal Research, 182*, 97–112.

Muñoz, G., Weckmann, U., Pek, J., Kováčiková, S., & Klanica, R. (2018). Regional two-dimensional magnetotelluric profile in West Bohemia/Vogtland reveals deep conductive channel into the earthquake swarm region. *Tectonophysics, 727*, 1–11. https://doi.org/10.1016/j.tecto.2018.01.012

Nickschick, T., Flechsig, C., Meinel, C., Mrlina, J., & Kämpf, H. (2017). Architecture and temporal variations of a terrestrial CO_2 degassing site using electric resistivity tomography and self-potential. *International Journal of Earth Sciences, 106*, 2915–2926. https://doi.org/10.1007/s00531-017-1470-0

Nickschick, T., Flechsig, C., Mrlina, J., Oppermann, F., Löbig, F., & Günther, T. (2019). Large-scale electrical resistivity tomography in the Cheb Basin (Eger Rift) at an International Continental Drilling Program (ICDP) monitoring site to image fluid-related structures. *Solid Earth, 10*, 1951–1969. https://doi.org/10.5194/se-10-1951-2019

Nickschick, T., Kaempf, H., Flechsig, C., Mrlina, J., & Heinicke, J. (2015). CO2 degassing in the Hartousov mofette area, western Eger Rift, imaged by CO_2 mapping and geoelectrical and gravity surveys. *International Journal of Earth Sciences, 104*, 2107–2129.

Özyıldırım, Ö., Candansayar, M. E., Demirci, İ, & Tezkan, B. (2017). Two-dimensional inversion of magnetotelluric/radiomagnetotelluric data by using unstructured mesh. *Geophysics, 82*(4), E197–E210. https://doi.org/10.1190/geo2016-0378.1

Pedersen, L. B., Juhlin, C., & Rasmussen, T. M. (1992). Electric resistivity in the Gravberg-1 deep well, Sweden. *Journal of Geophysical Research: Solid Earth, 97*, 9171–9182. https://doi.org/10.1029/91JB02991

Platz, A., Weckmann, U., Pek, J., Kováčiková, S., Klanica, R., Mair, J., & Aleid, B. (2022). 3D imaging of the subsurface electrical resistivity structure in West Bohemia/Upper Palatinate covering mofettes and Quaternary volcanic structures by using Magnetotellurics. *Tectonophysics*. https://doi.org/10.1016/j.tecto.2022.229353

Plomerová, J., Achauer, U., Babuška, V., Vecsey, L., Kämpf, H., Bräuer, K., Schumann, J., et al. (2013). CO_2 discharge in an active, non-volcanic continental rift area (Czech Republic): Characterisation (δ13C, 3He/4He) and quantification of diffuse and vent CO_2 emissions. *Chemical Geology, 339*, 71–83. https://doi.org/10.1016/j.chemgeo.2012.08.005

Prodehl, C., Müller, S., & Haak, V. (1995). The European Cenozoic rift system. *Continental rifts: Evolution, structure, tectonics. Developments in Geotectonics* (pp. 133–212). Elsevier.

Ritter, O., Junge, A., & Dawes, G. (1998). New equipment and processing for magnetotelluric remote reference observations. *Geophysical Journal International, 132*, 535–548.

Rohrmüller, J., Kämpf, H., Geiß, E., Großmann, J., Grun, I., Mingram, J., Mrlina, J., Plessen, B., Stebich, M., Veress, C., Wendt, A., & Nowaczyk, N. (2017). Reconnaissance study of an inferred Quaternary maar structure in the western part of the Bohemian Massif near Neualbenreuth, NE-Bavaria (Germany). *International Journal of Earth Sciences, Springer Science and Business Media LLC, 107*, 1381–1405.

Rulff, P. (2018). Radiomagnetotellurics for imaging mofette structures in the Eger Rift System, Czech Republic—A comparative study. MSc Thesis, University of Potsdam.

Růzek, B., & Horálek, J. (2013). Three-dimensional seismic velocity model of the west Bohemia/Vogtland seismoactive region. *Geophysical Journal International, 195*, 1251–1266. https://doi.org/10.1093/gji/ggt295

Saraev, A., Simakov, A., Tezkan, B., Tokarev, I., & Shlykov, A. (2020). On the study of industrial waste sites on the Karelian Isthmus/Russia using the RMT and CSRMT methods. *Journal of Applied Geophysics, 175*, 103993. https://doi.org/10.1016/j.jappgeo.2020.103993

Sauer, U., Watanabe, N., Singh, A., Dietrich, P., Kolditz, O., & Schütze, C. (2014). Joint interpretation of geoelectrical and soil-gas measurements for monitoring CO_2 releases at a natural analogue. *Near Surface Geophysics, 12*, 165–178. https://doi.org/10.3997/1873-0604.2013052

Schunk, R., Peterek, A., & Reuther, C. D. (2005) Second day: Active processes of the western Eger Graben system, Stop 6a-c. In: Kämpf, H., Peterek, A., Rohrmüller, J., Kümpel, Hj., Geissler, W. (Eds) The KTB Deep Crustal Laboratory and the Western Eger Graben. *Schriftreihe Dt Ges Geowiss, 40*, 66–71.

Schütze, C., Sauer, U., Beyer, K., Lamert, H., Bräuer, K., Strauch, G., Flechsig, C., et al. (2012). Natural analogues: A potential approach for developing reliable monitoring methods to understand subsurface CO_2 migration processes. *Environment and Earth Science, 67*, 411–423. https://doi.org/10.1007/s12665-012-1701-4

Schwalenberg, K., Rath, V., & Haak, V. (2002). Sensitivity studies applied to a two-dimensional resistivity model from the Central Andes. *Geophysical Journal International, 150*, 673–686. https://doi.org/10.1046/j.1365-246X.2002.01734.x

Spies, B. R. (1989). Depth of investigation in electromagnetic sounding methods. *Geophysics, 54*, 872–888.

Tezkan, B. (2009). Radiomagnetotellurics. In R. Kirsch (Ed.), *Groundwater geophysics.* Springer. https://doi.org/10.1007/978-3-540-88405-7_10

Ulrych, J., Cajz, V., Pivec, E., et al. (2000). Cenozoic intraplate alkaline volcanism of Western Bohemia. *Studia Geophysica Et*

Geodaetica, 44, 346–351. https://doi.org/10.1023/A:1022131413783

Ulrych, J., Dostal, J., Adamovič, J., Jelínek, E., Špaček, P., Hegner, E., & Balogh, K. (2011). Recurrent Cenozoic volcanic activity in the Bohemian Massif (Czech Republic). *Lithos, 123*(1–4), 133–144.

Vizheh, M., Oskooi, B., & Bastani, M. (2020). Using GPR data as constraints in RMT data inversion for water content estimation: A case study in Heby, Sweden. *Pure and Applied Geophysics, 177*, 2903–2929. https://doi.org/10.1007/s00024-019-02391-1

Wang, S., Malehmir, A., & Bastani, M. (2016). Geophysical characterization of areas prone to quick-clay landslides using radio-magnetotelluric and seismic methods. *Tectonophysics, 677–678*, 248–260. https://doi.org/10.1016/j.tecto.2016.04.020

Weckmann, U., Magunia, A., & Ritter, O. (2005). Effective noise separation for magnetotelluric single site data processing using a frequency domain selection scheme. *Geophysical Journal International, 161*, 635–652.

Weidelt, P., & Kaikkonen, P. (1994). Local 1-D interpretation of magnetotelluric B-polarisation impedances. *Geophysical Journal International, 17*, 733–748.

Weinlich, F. H., Bräuer, K., Kämpf, H., Strauch, G., Tesař, J., & Weise, S. M. (1999). An active subcontinental mantle volatile system in the western Eger rift, Central Europe: Gas flux, isotopic (He, C, and N) and compositional fingerprints. *Geochimica Et Cosmochimica Acta, 63*(21), 3653–3671.

Woith, H., Vlček, J., Vylita, T., Dahm, T., Fischer, T., Daskalopoulou, K., Zimmer, M., et al. (2022). Effect of pressure perturbations on CO_2 degassing in a mofette system: The case of Hartoušov, Czech Republic. *Geosciences, 13*, 2. https://doi.org/10.3390/geosciences13010002

Yan, P., Garcia Juanatey, M. A., Kalscheuer, T., Juhlin, C., Hedin, P., Savvaidis, A., Lorenz, H., et al. (2017). A magnetotelluric investigation of the Scandinavian Caledonides in western Jämtland, Sweden, using the COSC borehole logs as prior information. *Geophysical Journal International, 208*, 1465–1489. https://doi.org/10.1093/gji/ggw457

Yang, X., Lassen, R. N., Jensen, K. H., & Looms, M. C. (2015). Monitoring CO migration in a shallow sand aquifer using 3D crosshole electrical resistivity tomography. *International Journal of Greenhouse Gas Control, 42*, 534–544.

Yogeshwar, P., Tezkan, B., Israil, M., & Candansayar, M. E. (2012). Groundwater contamination in the Roorkee area, India: 2D joint inversion of radiomagnetotelluric and direct current resistivity data. *Journal of Applied Geophysics, 76*, 127–135. https://doi.org/10.1016/j.jappgeo.2011.11.001

Ziegler, P. A. (1992). Plate tectonics, plate moving mechanisms and rifting. *Tectonophysics, 215*, 9–34. https://doi.org/10.1016/0040-1951(92)90072-E

(Received March 6, 2024, revised October 28, 2024, accepted January 20, 2025)